Tidally modulated temperature observed atop a drillsite at the Noho hydrothermal site, mid-Okinawa Trough

Masataka Kinoshita[1], Kazuya Kitada[2], and Tatsuo Nozaki[3]

[1]University of Tokyo
[2]Japan Agency for Marine-Earth Science and Technology (JAMSTEC)
[3]JAMSTEC

November 22, 2022

Abstract

We observed temperature variations over 10 months within a Kuroko ore (hydrothermal sulfide) cultivation apparatus installed atop a 50-m-deep borehole drilled in the Noho hydrothermal system in the mid-Okinawa Trough, southwestern Japan, for monitoring of hydrothermal fluids and in situ mineral precipitation experiments. Temperature and pressure in the apparatus fluctuated with the tidal period immediately after its installation. Initially, the average temperature was 75–76 °C and the amplitude of the semi-diurnal tidal temperature modulation was ~0.3 °C. Four months later, the amplitude of tidal temperature modulation had gradually increased to 4 °C in synchrony with an average temperature decrease to ~40 °C. Numerical modeling showed that both the increase in tidal amplitude and the decrease in average temperature were attributable to a gradual decrease in inflow to the apparatus, which promoted conductive cooling through the pipe wall. The reduced inflow was probably caused by clogging inside the apparatus, but we cannot rule out a natural cause, because the drilling would have significantly decreased the volume of hot fluid in the reservoir. The temperature fluctuation phase lagged the pressure fluctuation phase by ~150°. Assuming that the fluctuations originated from inflow from the reservoir, we conducted 2-D numerical hydrothermal modeling for a poroelastic medium. To generate the 150° phase lag, the permeability in the reservoir needed to exceed that in the ambient formation by ~3 orders of magnitude. The tidal variation phase can be a useful tool for assessing the hydrological state and response of a hydrothermal system.

Hosted file

`agu_suppinfo_word.docx` available at https://authorea.com/users/537440/articles/599334-tidally-modulated-temperature-observed-atop-a-drillsite-at-the-noho-hydrothermal-site-mid-okinawa-trough

Hosted file

`movie_s3.gif` available at https://authorea.com/users/537440/articles/599334-tidally-modulated-temperature-observed-atop-a-drillsite-at-the-noho-hydrothermal-site-mid-okinawa-trough

Hosted file

`movie_s2.gif` available at https://authorea.com/users/537440/articles/599334-tidally-modulated-temperature-observed-atop-a-drillsite-at-the-noho-hydrothermal-site-mid-okinawa-trough

Tidally modulated temperature observed atop a drillsite at the Noho hydrothermal site, mid-Okinawa Trough

Masataka Kinoshita[1, 2], Kazuya Kitada[3] and Tatsuo Nozaki[2,4,5,6]

[1] Earthquake Research Institute, The University of Tokyo, 1-1-1 Yayoi, Bunkyo-ku, Tokyo 113-0032, Japan

[2] Submarine Resources Research Center, Research Institute for Marine Resources Utilization (MRU), Japan Agency for Marine-Earth Science and Technology (JAMSTEC), 2-15 Natsushima-cho, Yokosuka, Kanagawa 237-0061, Japan

[3] Advanced Science-Technology Research (ASTER) Program, Institute for Extra-cutting-edge Science and Technology Avant-garde Research (X-star), Japan Agency for Marine-Earth Science and Technology (JAMSTEC), 2-15 Natsushima-cho, Yokosuka, Kanagawa 237-0061, Japan

[4] Frontier Research Center for Energy and Resources (FRCER), The University of Tokyo, 7-3-1 Hongo, Bunkyo-ku, Tokyo 113-8656, Japan

[5] Department of Planetology, Graduate School of Science, Kobe University, 1-1 Rokkodai-cho, Nada-ku, Kobe, Hyogo 657-8501, Japan

[6] Ocean Resources Research Center for Next Generation, Chiba Institute of Technology, 2-17-1 Tsudanuma, Narashino, Chiba 275-0016, Japan

Corresponding author: Masataka Kinoshita (masa@eri.u-tokyo.ac.jp)

Key Points:

- Temperature and pressure atop a borehole in the mid-Okinawa Trough hydrothermal system fluctuated with the tidal period during 10 months.
- The temperature tidal fluctuation phase lagged pressure by ~150° likely because of the poroelastic response of higher permeability sediment.
- A gradual temperature decrease and tidal amplitude increase were caused by reduced inflows that promoted conductive cooling.

Index Terms and Keywords:

- hydrothermal circulation, tidal modulation, permeability, Kuroko ore-cultivation apparatus, borehole observatory, CK16-01 (D/V Chikyu Expedition 908)

Abstract

We observed temperature variations over 10 months within a Kuroko ore (hydrothermal sulfide) cultivation apparatus installed atop a 50-m-deep borehole drilled in the Noho hydrothermal system in the mid-Okinawa Trough, southwestern Japan, for monitoring of hydrothermal fluids and in situ mineral precipitation experiments. Temperature and pressure in the apparatus fluctuated with the tidal period immediately after its installation. Initially, the average temperature was 75–76 °C and the amplitude of the semi-diurnal tidal temperature modulation was ~0.3 °C. Four months later, the amplitude of tidal temperature modulation had gradually increased to 4 °C in synchrony with an average temperature decrease to ~40 °C. Numerical modeling showed that both the increase in tidal amplitude and the decrease in average temperature were attributable to a gradual decrease in inflow to the apparatus, which promoted conductive cooling through the pipe wall. The reduced inflow was probably caused by clogging inside the apparatus, but we cannot rule out a natural cause, because the drilling would have significantly decreased the volume of hot fluid in the reservoir. The temperature fluctuation phase lagged the pressure fluctuation phase by ~150°. Assuming that the fluctuations originated from inflow from the reservoir, we conducted 2-D numerical hydrothermal modeling for a poroelastic medium. To generate the 150° phase lag, the permeability in the reservoir needed to exceed that in the ambient formation by ~3 orders of magnitude. The tidal variation phase can be a useful tool for assessing the hydrological state and response of a hydrothermal system.

Plain Language Summary

Subseafloor magmatic activity causes vigorous fluid flow, called hydrothermal circulation, between magma and seawater. Hot hydrothermal fluid vented at the seafloor often contains many valuable metals and minerals, which precipitate instantly when the fluid is released into the cold seawater. The Kuroko ore-cultivation project envisions collecting these metals and minerals by drilling into a hydrothermal reservoir and deploying an artificial cultivation apparatus atop the borehole. In this study, we aimed to characterize the behavior of the captured fluid by continuously monitoring temperature and pressure in the cultivation apparatus. We successfully obtained a 10-month-long data series from atop a 50-m-deep borehole drilled in the Noho hydrothermal system in the mid-Okinawa Trough, southwestern Japan. Initially, the hot fluid (~76 °C) flowed freely through the cultivation apparatus, but after about 4 months, the inflow dropped significantly, probably because of clogging inside the apparatus. The reduction in flow causes conductive cooling of the fluid to ~40 °C, and the amplitude of the tidally modulated temperature variation also increased. The phase difference between the pressure and temperature variations allowed us to infer the permeability of the reservoir. We propose that the Noho hydrothermal system has higher permeability than the surrounding materials.

1. Introduction

The Okinawa Trough, which extends 1,200 km between the Ryukyu Island chain and the East China Sea, is the backarc basin of the Ryukyu trench–arc system. Seismic reflection data have shown that an igneous basement layer between 1,000 and 6,000 meters below the seafloor (mbsf) is overlain by a 1,000-m-thick layer of terrigenous hemipelagic sediments (Letouzey & Kimura, 1986) mainly derived from the Asian continent.

The evolution of the Okinawa Trough has been investigated during the past ~40 years by intensive geological and geophysical surveys (e.g., Kimura, 1985; Lee et al., 1980; Letouzey & Kimura, 1985, 1986; Liu et al., 2016; Sibuet et al., 1987, 1998; Zhang et al., 2019). Liu et al. (2016) performed a synthesis of geophysical data and interpreted the central and southern Okinawa Trough to be at the early stage of backarc spreading, but Arai et al. (2017), who analyzed active seismic survey data, suggested that the southern Okinawa Trough is in a transitional stage from continental rifting to seafloor spreading. Heat flow data are key to constraining the evolution of the Okinawa Trough. So far as is known, the heat flow in the Okinawa Trough ranges from less than 40 mW/m^2 to higher than 200 mW/m^2. Zhang et al. (2019) interpreted the heat flow data by considering the effects of rapid sedimentation and mantle upwelling, However, a lack of adequate regional heat flow data prevents a full understanding of the evolutionary history of the Okinawa Trough.

Various active hydrothermal sites have been discovered and explored in the Okinawa Trough (e.g., Glasby and Notsu, 2003; Halbach et al., 1989; Ishibashi & Urabe, 1995; Ishibashi et al., 2015; Kawagucci et al., 2010; Kimura et al., 1988; Kinoshita & Yamano, 1997; Kinoshita et al., 1990; Nozaki et al., 2021a, 2021c; Sakai et al., 1990; Takai et al., 2011, 2012; Yamano et al., 1989). According to Masaki et al. (2011), who analyzed heat flow data from 78 sites in the

Iheya-North hydrothermal field in the mid-Okinawa Trough obtained by remotely operated vehicle (ROV) dive surveys, heat flow within the active hydrothermal area varies greatly from 0.01 to 10 W/m^2 whereas heat flow on the eastern sedimented slope is 0.1–1 W/m^2. Farther east, where the covering sediments are coarser, the extremely low heat flow (<0.1 W/m^2) suggests seawater recharge into the subseafloor. This low heat flow was confirmed during the Integrated Ocean Drilling Program (IODP) Expedition (Exp.) 331 Deep Hot Biosphere cruise of D/V *Chikyu* (Takai et al., 2011, 2012), conducted in 2010 in the Iheya-North hydrothermal field.

The Noho hydrothermal site is in the mid-Okinawa Trough on the south side of the Iheya Minor Ridge, ~30 km south of the Iheya-North hydrothermal field (Figure 1). Miyazaki et al. (2017) reported the temperature of the hydrothermal vent fluid at this site to be 331 °C. Under the Strategic Innovation Program (SIP) of the Japanese Cabinet Office, a Kuroko ore (hydrothermal sulfide) cultivation apparatus for long-term monitoring of hydrothermal fluids and for performing an in situ mineral precipitation experiment (Nozaki, 2017) was installed atop the drilled Hole C9017B from March to December 2016 during cruise CK16-01 (D/V *Chikyu* Exp. 908) (Figure 1c).

Hole C9017B was drilled to 50 mbsf, and a screened casing pipe was installed to ~20 mbsf (Figure 2a, b). The hydrothermal precipitates recovered so far have been petrographically and geochemically analyzed (Nozaki et al., 2019), but the physical conditions within the system (temperature, pressure, flow rate) have not yet been explored. In this paper, we describe the secular fluctuations of these parameters and investigate their possible causes by conducting analytical and numerical simulations.

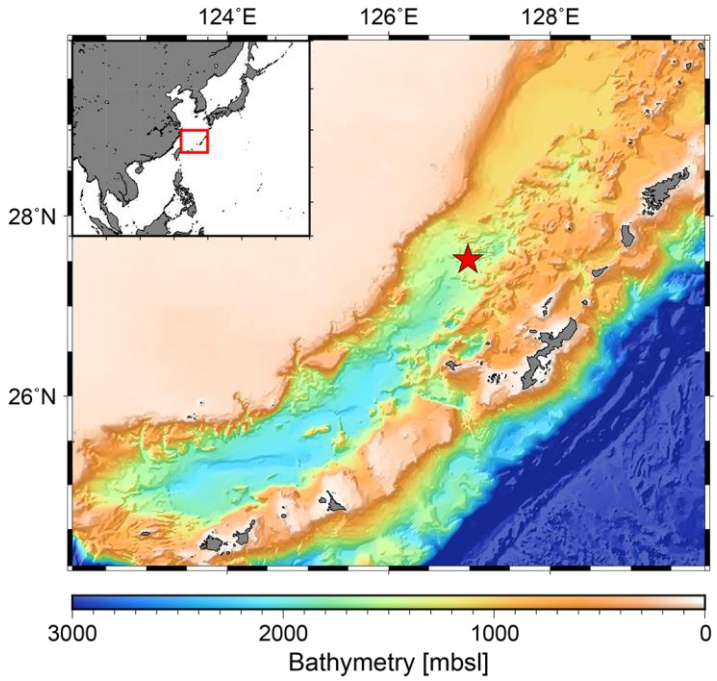
124°E
126°E
128°E
28°N
26°N
3000
2000
1000
0
Bathymetry [mbsl]

(a)

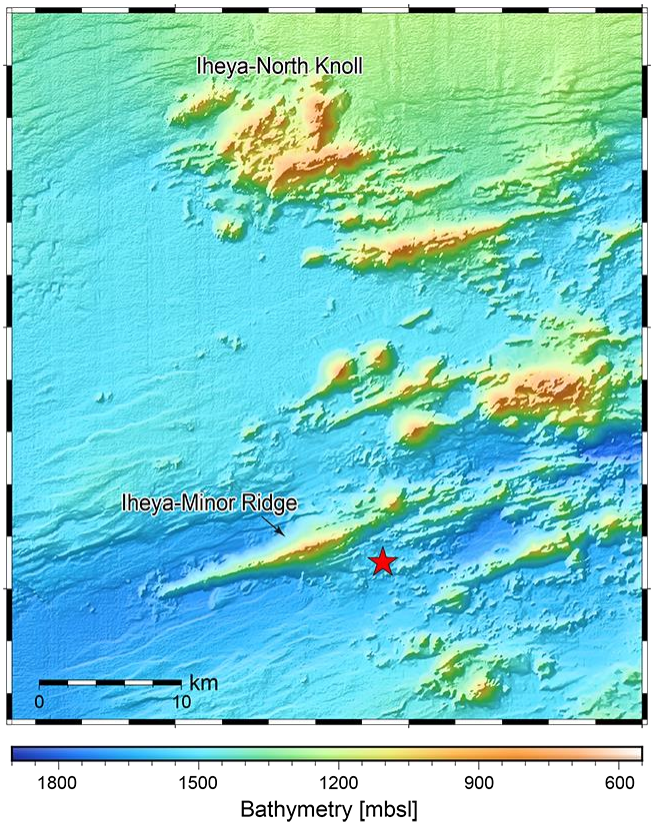
Iheya-North Knoll
Iheya-Minor Ridge
km
0
10
1800
1500
1200
900
600
Bathymetry [mbsl]

(b)

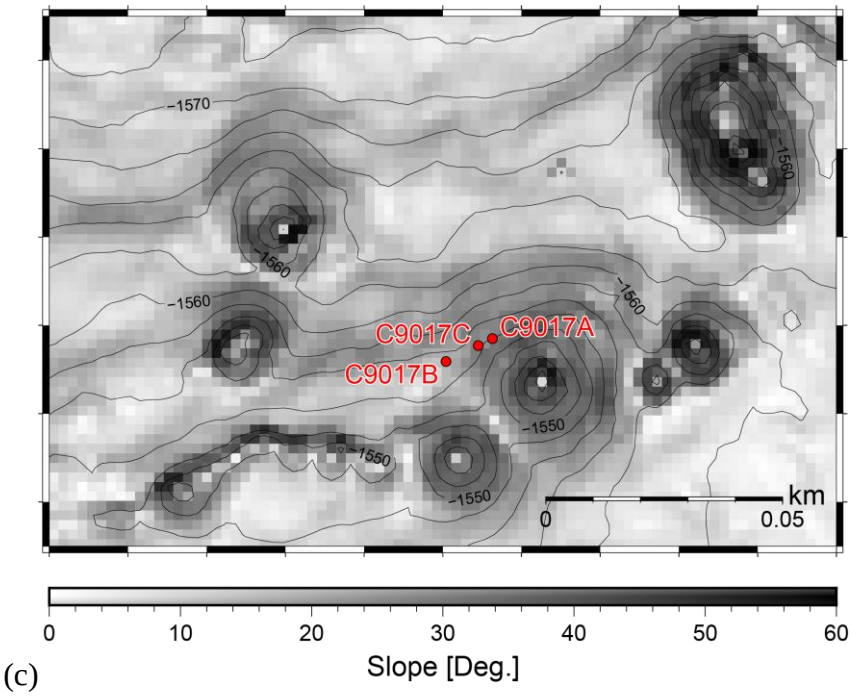

(c)

Figure 1. (a) Bathymetric map of the Okinawa Trough. The red star indicates the location of the Noho hydrothermal site in the mid-Okinawa Trough. The inset map shows the regional location of the Okinawa Trough. (b) Bathymetric map of the mid-Okinawa Trough constructed with bathymetric data from Komori et al. (2017) and Kasaya et al. (2020). The red star indicates the location of the Noho hydrothermal site. (c) Seafloor gradient map of the Noho hydrothermal site showing drillhole sites. The bathymetric contour interval is 2 m.

1.1. Previous studies

Temporal variations of hydrothermal fluid temperature, pressure, and flow rates and of bottom currents have been studied at various seafloor hydrothermal venting sites. They include analyses of tidally modulated variations (i.e., amplitude decay and phase lag).

In the northern Cleft Segment of the Juan de Fuca Ridge, Tivey et al. (2002) observed modulations of temperature and total radioactivity associated with tidally induced changes in bottom currents. Larson et al. (2007) reported tidal influences on temperature and Cl concentration at a high-temperature (>300 °C) vent on Juan de Fuca Ridge. At the active TAG hydrothermal mound on the Mid-Atlantic Ridge, Sohn (2007a, 2007b) interpreted semidiurnal tidal modulations in a one-year time series of exit fluid temperatures at diffuse sites as being due to poroelastic effects from tidal loading. Sawyer et al. (2008) examined borehole pressure data from near the toe of the Nankai Trough at a convergent boundary and used tidal response data to estimate hydraulic properties.

Barreyre et al. (2014) measured temperature, pressure, and bottom currents at the Lucky Strike hydrothermal field on the Mid-Atlantic Ridge for three years and reported that temperature records from high- (>190 °C), intermediate (10–100 °C), and low-temperature (<10 °C) outflows exhibited variations corresponding to semi-diurnal tidal variations. They also showed that the phase of the tidally modulated temperature variation was almost the inverse of that of the pressure variation. Barreyre and Sohn (2016) found differences in the phase lag in temperature data from active vents of three hydrothermal systems (Lucky Strike, East Pacific Rise, and Main Endeavour fields). Crone and Wilcock (2005), who conducted both analytical and numerical modeling of tidal loading in a poroelastic half-space, demonstrated that tides generate significant vertical and horizontal pressure gradients in mid-oceanic hydrothermal systems and inferred that significant tidal mixing and fluid exchange occur below the seafloor.

Jupp and Schultz (2004) applied the theory of poroelasticity to predict the magnitude and phase of tidally induced changes in the temperature and flow rate of hydrothermal effluent at the seafloor. We further discuss their analytical results in Section 4.

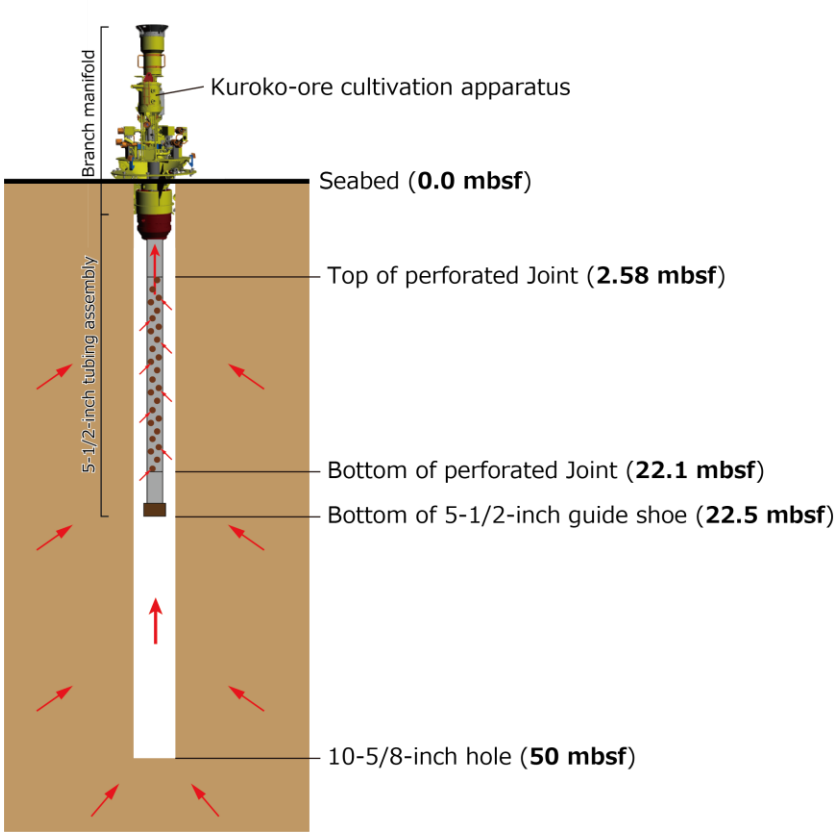
Branch manifold
Kuroko-ore cultivation apparatus
Seabed (**0.0 mbsf**)
5-1/2-inch tubing assembly
Top of perforated Joint (**2.58 mbsf**)
Bottom of perforated Joint (**22.1 mbsf**)
Bottom of 5-1/2-inch guide shoe (**22.5 mbsf**)
10-5/8-inch hole (**50 mbsf**)

(a)

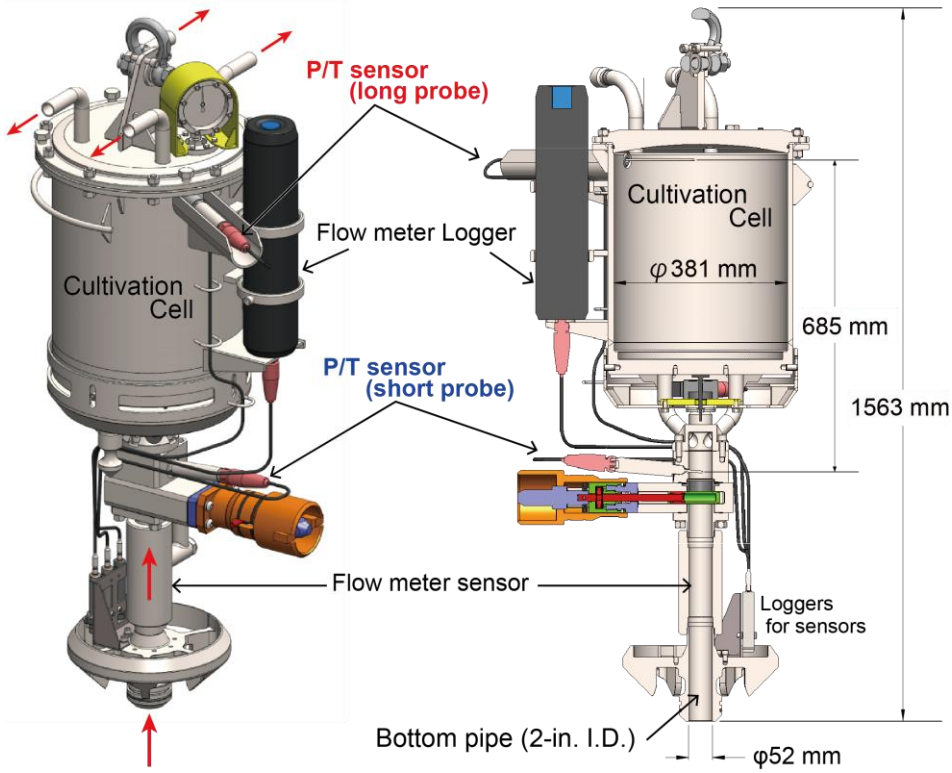
P/T sensor
(long probe)
Flow meter Logger
Cultivation
Cell
P/T sensor
(short probe)
Flow meter sensor
Cultivation
Cell
φ381 mm
685 mm
1563 mm
Loggers
for sensors
Bottom pipe (2-in. I.D.)
φ52 mm

(b)

(c)

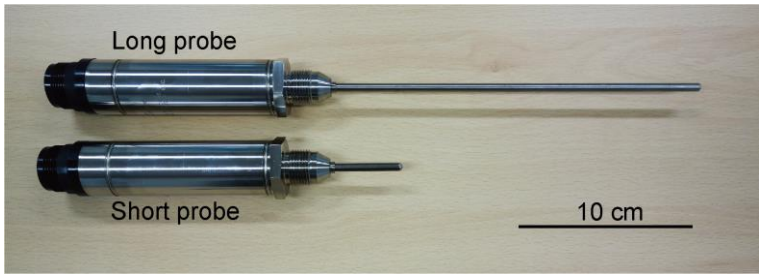

(d)

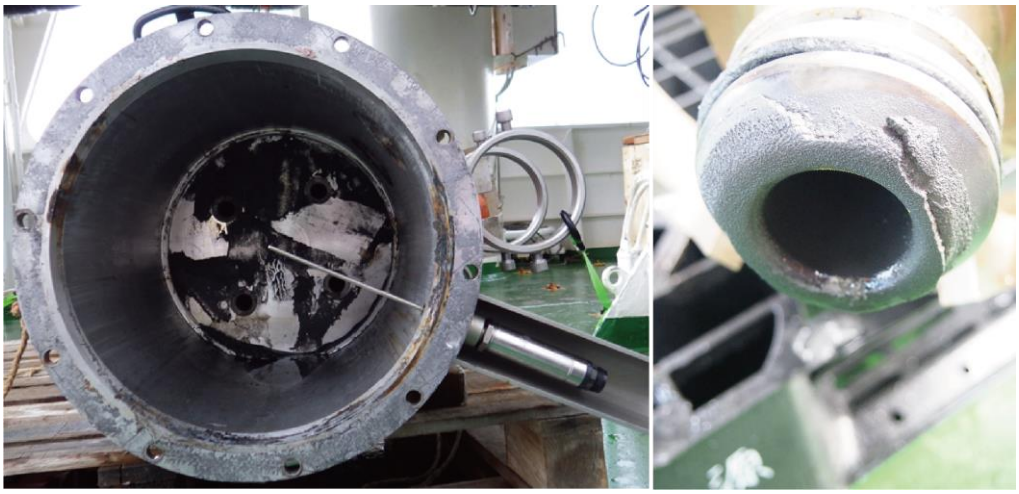

Figure 2. The Kuroko ore-cultivation apparatus deployed in Hole C9017B at the Noho hydrothermal site, mid-Okinawa Trough. (a) Cross-sectional view of Hole C9017B. The borehole diameter was 10-5/8 inches, and the bottom depth was about 50 mbsf. The apparatus was attached to a perforated joint about 22 m long within the borehole. The diameter of the perforated joint was 5-1/2 inches. The red arrows indicate hydrothermal flows. (b) Configuration of the Kuroko ore-cultivation apparatus. A long-probe pressure/temperature (*P*/*T*) sensor was mounted at the top center of the cultivation cell, and a short-probe *P*/*T* sensor and flow meter were attached to the inside of the 2-inch ID bottom pipe. Hydrothermal fluid flowing through the bottom pipe exited via four outlets at the top of the cultivation cell. (c) Photograph of the long- and short-probe *P*/*T* sensors. See Table 2 for their specifications. (d) Photographs of the cultivation cell (left) and the 2-inch bottom pipe (right) after their recovery from Hole C9017B during the KR16-17 cruise. The long-probe *P*/*T* sensor can be seen in the cell.

2. Observations and Methods

2.1. Operation Summary

From 11 February to 17 March 2016, drilling cruise CK16-01 (D/V *Chikyu*; Exp. 908) was conducted at hydrothermal fields in the mid-Okinawa Trough to investigate the subseafloor geological structure and the genesis of polymetallic sulfide mineralization. During the cruise, Kuroko ore-cultivation apparatuses were installed at Noho (site C9017) and Iheya-North Knoll (site C9024) to monitor pressure, temperature, and the flow rate of hydrothermal fluids discharged from artificial hydrothermal vents (Kawagucci et al., 2013; Nozaki et al., 2016, 2021b; Takai et al., 2012).

At Noho site, Hole C9017B was drilled at a water depth of 1,557.5 meters below sea level (mbsl) with a 10-5/8-inch bottom hole assembly to a total depth of 50.0 mbsf on 27 February 2016. Hole C9017B is only 13 m WSW from Hole C9017A, which was drilled in a logging-while-drilling (LWD) operation and where vigorous hydrothermal discharge was observed after pull out from the hole (Figure 1c). After drilling, a Kuroko ore-cultivation apparatus was connected to the top of a 5-1/2-inch tubing assembly, which included a perforated joint (from 2.58 to 22.1 mbsf), that ran down to 22.5 mbsf in Hole C9017B. Note that this cultivation apparatus was installed directly on the seafloor without the tripod system nor the ROV platform (Kumagai et al., 2017), and there was a narrow annulus between the base of branch manifold and the open borehole (Figure 2a). After installation, hydrothermal discharge (shimmering) was observed from both steel vent pipes at the top of the cell and as basal leakage at the annulus (see supplementary Movie S1). About 10 months later, in January 2017, the cultivation cell, along with the sensors and their loggers, was recovered from Hole C9017B by

ROV *Kaiko Mk-IV* and R/V *Kairei* during cruise KR16-17. The operation logs at Site C9017 are summarized in Table 1.

Table 1. Operation logs at the Site C9017

Start Time [JST]		End Time [JST]		Cruise	Hole	Operation	Remarks
Feb/16/2016	14:30	Feb/17/2016	3:45	CK16-01	C9017A	Drilling (LWD, Logging While Drilling)	
Feb/27/2016	8:30	Feb/27/2016	16:00	CK16-01	C9017B	Drilling	
Feb/27/2016	23:00	Feb/28/2016	9:00	CK16-01	C9017B	Deployment of the Kuroko-ore cultivation apparatus	Without the tripod system nor the ROV platform
Mar/2/2016	6:52	Mar/4/2016	21:00	CK16-01	C9017C	Drilling (coring)	
Nov/29/2016	9:45	Nov/30/2016	7:00	CK16-05	C9017A	Deployment of the Kuroko-ore cultivation apparatus	
Jan/3/2017	10:27	Jan/10/2017	15:40	KR16-17	C9017B	Recovery of the Kuroko-ore cultivation apparatus	ROV Kaiko Dive#728
Feb/14/2018	12:54	Feb/14/2018	15:53	KR18-02C	C9017A	Recovery of the Kuroko-ore cultivation apparatus	ROV Kaiko Dive#766

Note that all the date and time are in Japanese Standard Time (JST: UTC+9).

Table 2. Specifications of the sensors and the cultivation apparatus

Item	P/T Sensor		Flow Meter	Cultivation Apparatus
Type	Long probe	Short probe		
Company	Paine Electronics, LCC		HOFFER FLOW CONTROLS, INC	NuStar Technologies Pte Ltd
Sensor Specification	Pressure transducer Platinum resistance temperature detector (IEC 751, Class A)		Turbine flowmeter	
Series Number	211-55-0060-05K0-0850	211-55-0060-05K0-0163		
Size	φ31.8 mm x 205.2 mm	φ31.8 mm x 379.7 mm	I.D.: 50.8 mm (2 inch) O.D.: φ95.25 mm (3.75 inch)	Height: 1563 mm Pipe I.D.: φ52 mm Cultivation cell I.D.: 381 mm
Measurement Range	0 to 34.474 MPa			
Operating Temperature	-40 to 315.556 ℃		-73 to 267 °C	
Error	**Total error** (non-linearity, hysteresis, and thermal effects): ±0.20 %FS		**Linearity**: ±0.5 % (±0.25 % typical) of reading over tabulated lenear flow range. **Repeatability**: ±0.1 % (±0.05 % typical) over tabulated repeatable range.	
Sampling Interval	2 min	2 min	1 min	
Start Time [JST]	Feb/27/2016 0:30	Feb/27/2016 0:25	Feb/26/2016 23:52	
End Time [JST]	Jan/3/2017 14:24	Jan/3/2017 14:07	Dec/5/2016 8:19	

Note that all the date and time are in Japanese Standard Time (JST: UTC+9).

2.2. The Kuroko Ore-Cultivation Apparatus

The Kuroko ore-cultivation apparatus (Figure 2b) is a system for long-term monitoring of hydrothermal fluid discharge from an artificial hydrothermal vent created by drilling (e.g., Masaki et al., 2017; Nozaki, 2017). The apparatus consists of three parts: a cultivation cell, an inflow pipe, and physical property sensors. Within the cell, hydrothermal minerals precipitate through conductive cooling of the hydrothermal fluid by cold ambient seawater. The inflow pipe connects the cell to the 5-1/2-inch tubing assembly (Figure 2b). Each apparatus is equipped with two *P*/*T* sensors (Paine Electronics, LCC) designed for a high-temperature environments, and one flow meter (see Table 2 for specifications). The *P*/*T* sensors are located inside the cultivation cell and in the top of the inflow pipe, which has a 2-inch inner diameter (ID). The flow meter is installed inside the inflow pipe (Figure 2b). These sensors monitor the pressure, temperature, and flow rate of hydrothermal fluids discharged from the artificial hydrothermal vent.

A *P*/*T* sensor with a short probe was inserted into the inflow pipe, and one with a long probe was inserted into the cultivation cell near its top (Figure 2c). The sampling interval of the *P*/*T* sensors was 2 min, and the observation period was from 27 February 2016 to 3 January 2017. The sampling interval of the flow meter was 1 min, and the observation period was only from 26 February to 5 December 2016 because of its insufficient internal memory capacity. Note that all times and dates are Japan Standard Time (JST: UTC+9 h).

The resolution of the pressure data, ~10 kPa, was too low to analyze the tidal variation, which has an amplitude of a few tens of kilopascals. We also observed cross-talk between the temperature and pressure observations (~0.25 kPa/°C). We therefore used theoretical tidal height estimates instead of the observed pressure variation (see Section 3.2).

240 ## 3. Results

241 In this section, we describe the temperature and pressure data and their secular variations
242 observed by the Kuroko ore-cultivation apparatus (summarized in Figure 3), as well as the video
243 observations recorded during ROV dive surveys.

244

245 ### 3.1. Visual Observations of Venting and the Recovered Apparatus

246 The ROV video recording shows vigorous venting from the four outlets at the top of the
247 cultivation cell beginning on 5 March (Figure 4a). The venting speed was roughly estimated as a
248 few tens of centimeters per second, or several tens of liters per minute. By 1 January 2017, when
249 the apparatus was recovered, the venting from the top vent pipes had greatly diminished (Figure
250 4c). Snapshots of the area around the base of branch manifold just before its recovery show weak
251 shimmering on 1 January 2017 (Figure 4b, d; see supplementary movies).

252 After recovery, the apparatus was carefully observed onboard (Figure 2d). Unfortunately,
253 the cell was almost empty; it contained only a small amount of hemi-pelagic sediment and
254 pumice fragments (Nozaki et al., 2017). The bottom end of the inflow pipe was covered with
255 gray precipitates, but no precipitation was observed within the pipe. However, one of the authors
256 (T. Nozaki) observed white materials flowing out of the apparatus during its recovery by the
257 ROV. We therefore suspect that precipitation in the pipe had clogged it before recovery.

258

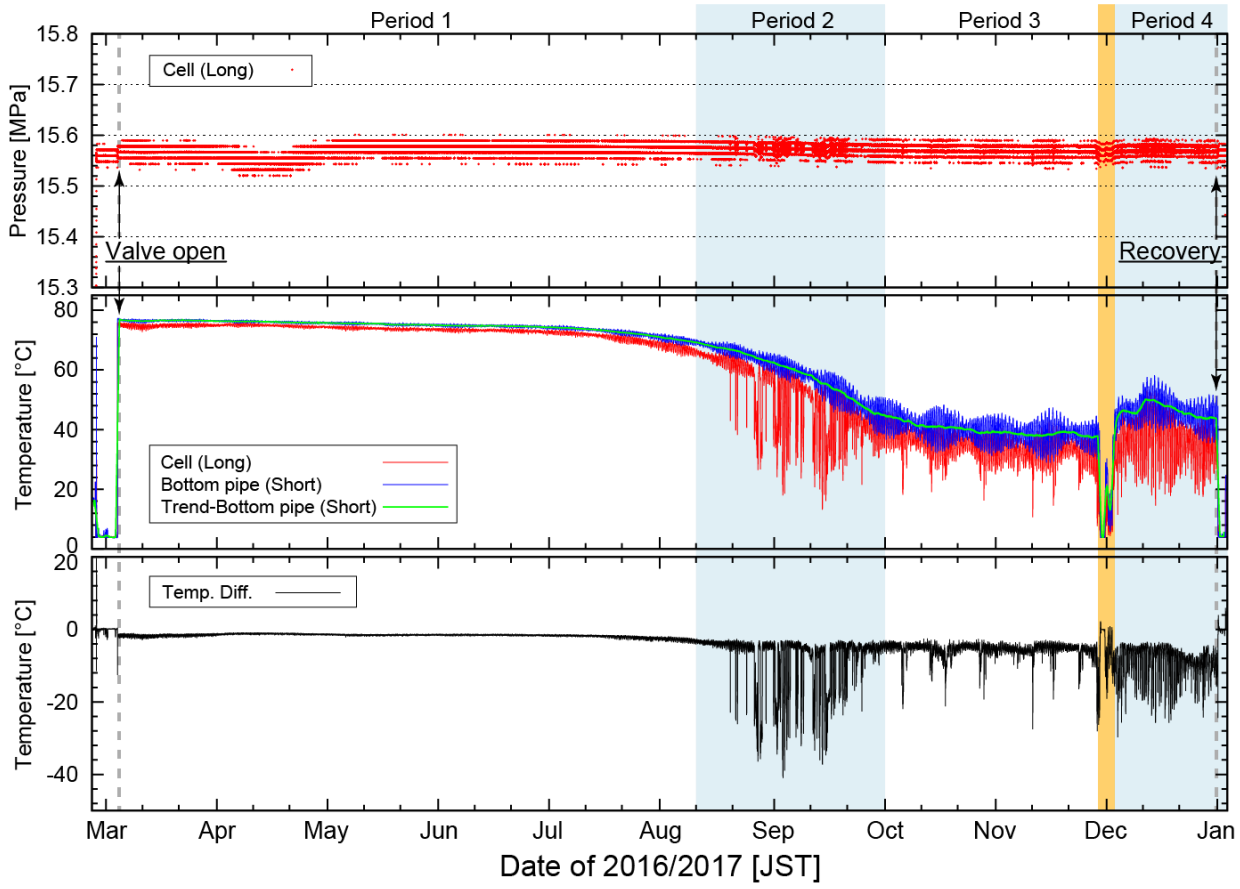

Figure 3. Temperature and pressure data recorded by the probes in the cell and the bottom inflow pipe during the whole observation period. (Top) Pressure in the cell. (Middle) Temperature in the cell and bottom inflow pipe. The green curve shows the running mean, with a window size of 24.84 hours (twice the period of the M2 tide), of the data from the probe in the bottom inflow pipe. (Bottom) The temperature difference between the probe in the cell and that in the bottom inflow pipe. All dates and times are Japanese Standard Time (JST: UTC+9).

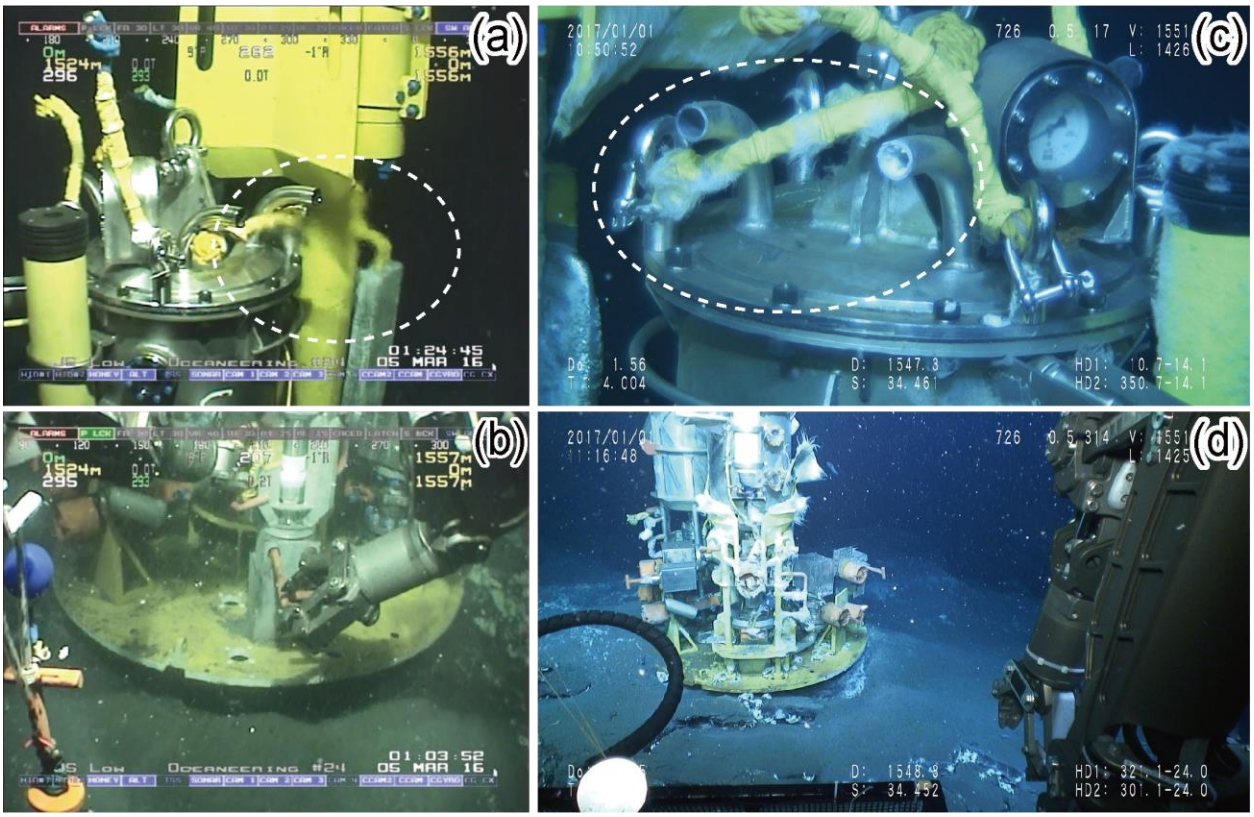

Figure 4. Snapshots of fluid venting from the Kuroko ore-cultivation apparatus in Hole C9017B. (a, b) Snapshots showing the status after installation on 5 March 2016. In (a), active hydrothermal flow is visible from the four outlets at the top of the apparatus, but no significant leakage from the basal part can be seen in (b). (c, d) Snapshots showing the status two days before recovery on 1 January 2017. In (c), weak flow is visible from the top outlet, and in (d) some shimmering is visible around the basal part.

3.2. Tidally Modulated Variations

3.2.1. Pressure Variations and Theoretical Tidal Heights

Pressure and temperature data were logged within the cell and the bottom inflow pipe (Figure 2). Pressure data logged by the short probe sensor in the bottom inflow pipe showed

283 obviously strange value so we disregarded it in our analyses. Pressure data logged within the cell
284 by the long probe sensor showed periodic variations around the constant baseline level for this
285 water depth, but as mentioned in Section 2.2, the resolution (Figure 5) was insufficient for
286 further analyses (e.g., for determining a phase shift with temperature data). Because these were
287 the only pressure data available from our *P/T* sensors, we substituted theoretical harmonic ocean
288 tide data calculated with the NAOTIDE program (Matsumoto et al., 2000) for observed pressure
289 in our analyses. NAOTIDE uses an ocean tide model developed by assimilating
290 TOPEX/POSEIDON altimeter data to predict ocean tidal height at a given time and location.

291 The observed amplitude of the pressure variation was roughly ±10 kPa (equivalent to a
292 sealevel height change of ±1 m), which agrees with the theoretical tidal amplitude (±70 cm)
293 (Figure 5). The phase difference between them was probably within 30 min and therefore
294 negligible. We thus used theoretical tide data as the pressure data in comparisons with
295 temperature data.

296

297 **3.2.2. Temperature Variations**

298 Temperatures recorded in the cultivation cell (long probe sensor) and in the bottom
299 inflow pipe (short probe sensor) were almost identical (Figure 5); their baseline levels and the
300 amplitude and phase of their periodic variations were the same. According to the characteristics
301 of the data, we divided the observation time series into four periods. During Period 1 (Figures 3,
302 5), the baseline (average) temperature was ~76 °C, and during Periods 2 and 3, it gradually
303 decreased to ~40 °C. The detailed features of each period are as follows:

304

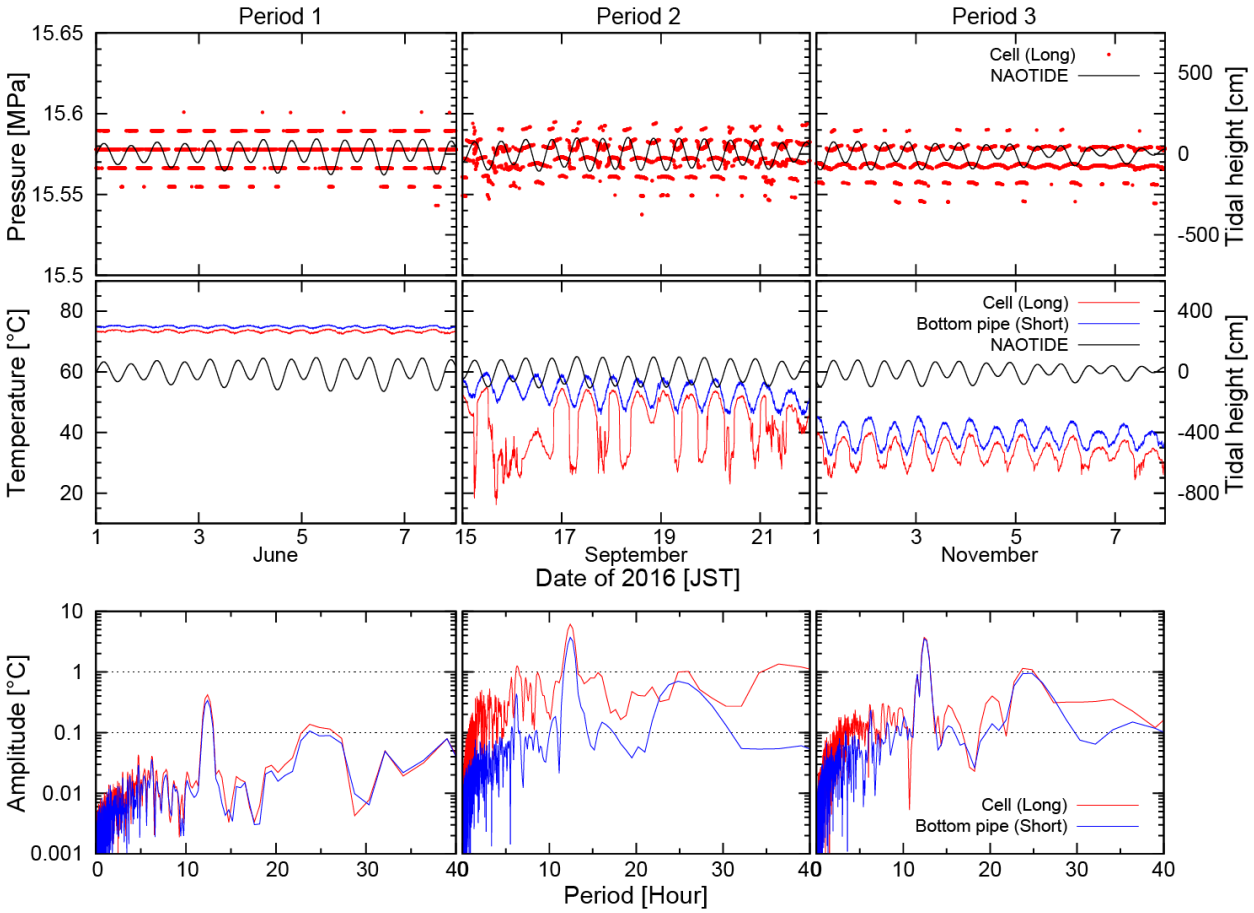

Figure 5. Enlarged views of pressure and temperature vs. time during Periods 1, 2, and 3. (Top) Measured pressure (red dots) and theoretical tidal height (black line). (Middle) Temperatures recorded by the long (red line) and short (blue line) probes. The theoretical tidal height (black line) is plotted for comparison. (Bottom) Amplitude spectrum of the temperature data. A fast Fourier transform (FFT) was applied to the data in 14-day windows. The amplitude of the temperature tidal variation clearly increased during Period 2.

316 *Period 1 (March–June 2016): High average temperature (~75 °C) that varied with a small,
317 constant periodic amplitude (about ±0.4 °C).

318 *Period 2 (July–September 2016): Temperature gradually decreased to ~40 °C, and the periodic
319 amplitude increased to about ±4 °C. The record of the long probe sensor in the cultivation cell
320 showed negative temperature excursions.

321 *Period 3 (October–November 2016): Low temperatures (<60 °C) and a large periodic amplitude
322 were maintained.

323 *Period 4 (December 2016 to January 2017): After a brief drop associated with nearby drilling at
324 Hole C9017A, the temperature recovered to ~40 °C with a large periodic amplitude. Negative
325 excursions recorded by the long-probe *P*/*T* sensor were larger than those during Periods 1–3.

326

327 The period of the periodic temperature variation appears to match that of the pressure
328 variation (NAOTIDE tide prediction) but with a phase lag (Figure 5). We used two methods to
329 estimate the amplitude and phase of the temperature variation in relation to pressure. The first
330 was to simply calculate their cross correlation, and, for the second, we applied the Baytap08
331 program to the temperature data to decompose them into tidal and non-tidal components
332 (Tamura & Agnew, 2008). For the Baytap08 calculation, we used the parameters "igrp = 3" to
333 fix the constituent grouping and "kind = 7", defined as the tide-generating potential divided by
334 the mean Earth radius and the acceleration due to gravity. For both methods, we used a time
335 window of 14 days and the window was shifted every 3 days. Although the Baytao08 program
336 decomposes the data into major tidal components (M2, O1, etc.), we extracted only the M2

337 component for further analysis. In the cross-correlation analysis, however, we included all tidal
338 components, but the correlation peak could be attributed to the M2 component.

339 The calculation results are shown in Figure 6. Phase lag values obtained by the two
340 methods agree well. The cell and bottom inflow pipe temperatures do not differ significantly and
341 show a constant phase lag of around 150° relative to theoretical tidal height. The amplitudes of
342 the temperature variations detected by the long and short probes agree well, except during Period
343 2 when the temperature at the top of the cell (long probe) showed repeated negative excursions.
344 These emerged after 20 August 2016 only in the temperatures detected by the long probe sensor
345 (Figures 3, 5). These negative temperature excursions, which always appeared during the "low-
346 temperature" period or the high-tide period, have amplitudes between –10 to –30 °C.

347

348 **3.2.3. Flow Velocity**

349 Unfortunately, volume flow data were obtained only for the first 10 h after deployment of
350 the Kuroko ore-cultivation apparatus (Figure 7, black curve). The data show a clear sinusoidal
351 variation with a period that is probably synchronized with the semi-diurnal (M2) tidal period.
352 Although the velocity data were obtained during less than one tidal cycle, their average and
353 amplitude can be estimated as ~70 L/min and ~3 L/min, respectively.

354 The flow velocity within the bottom inflow pipe (2-inch ID; where the short probe sensor
355 was set) was estimated to be ~60 ± 3 cm/s. The flow velocity agrees with those inferred from
356 visual observations (see Section 3.1).

357 The flow velocity phase lag is similar to that of temperature. According to Jupp and
358 Schultz (2004), velocity data can provide an important constraint on the hydrothermal circulation

regime. However, we did not use it in our analysis because the duration of the velocity data is too short to reliably assessment its phase.

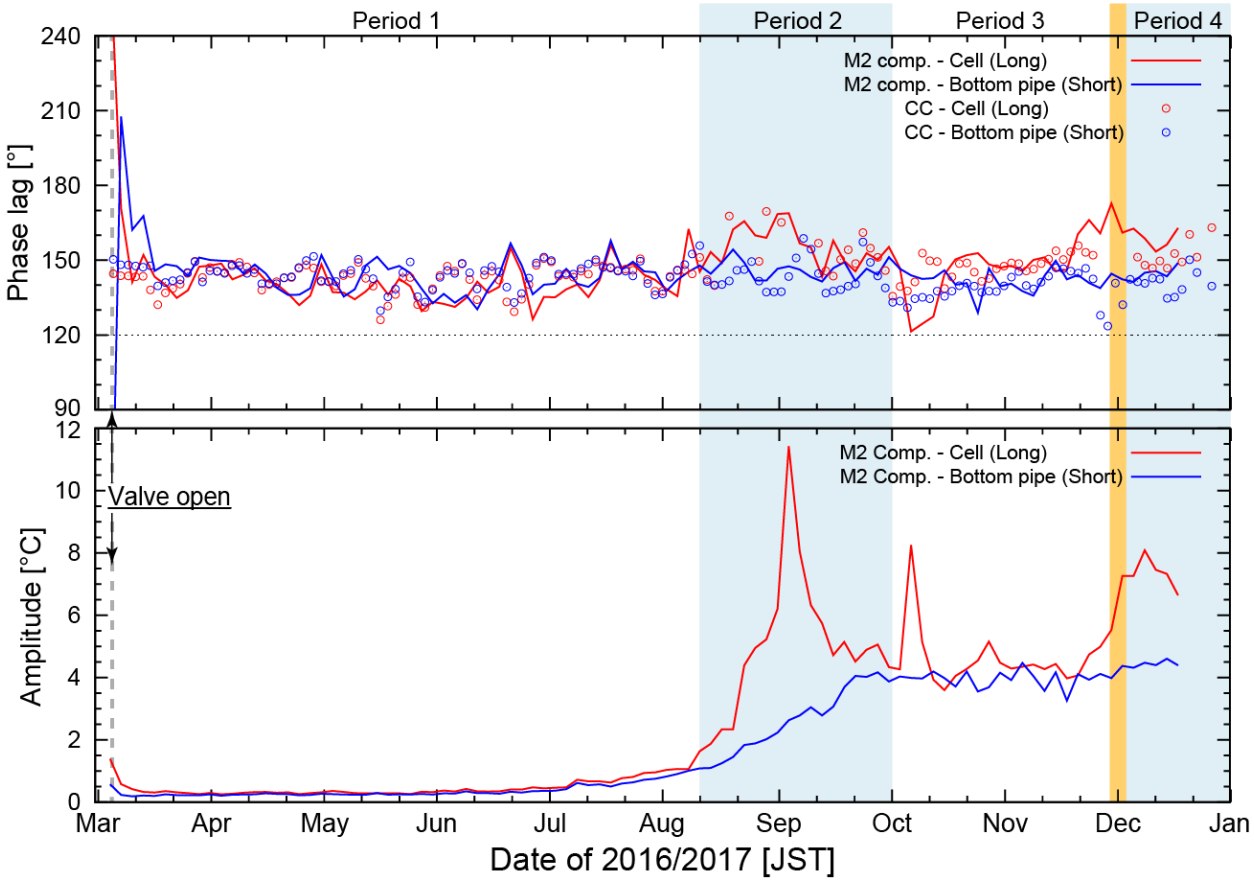

Figure 6. Time variation of the phase and amplitude of temperature data. The phase lag was calculated relative to the M2 component of the theoretical tidal height (NAOTIDE). Solid curves were derived with the Baytap08 program, and open circles were obtained by cross correlation, both using a time window of 14 days and a shift of 3 days. The phase lag is more or less constant at around 150° ± 10°, and no significant change in the phase lag was observed after installation of the apparatus.

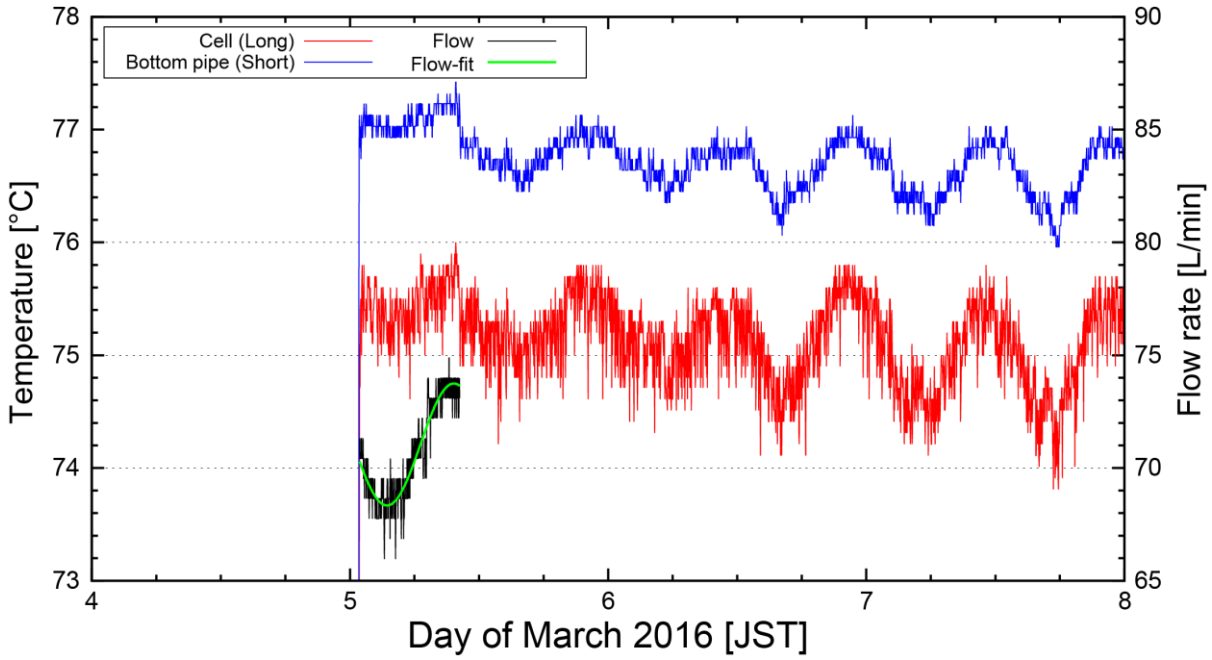

Figure 7. Flow velocity data (black line) and temperature records (blue and red lines) during the period immediately after deployment of the apparatus. The green curve is a sinusoidal fit to the velocity data. Although the velocity data were obtained during less than one tidal cycle, their average and half-amplitude could be estimated as ~70 L/min and ~3 L/min, respectively.

3.3. Step Change after Deployment

The Kuroko ore-cultivation apparatus was installed in Hole 9017B (Figure 2a) at ~05:00 JST on 28 February 2016, and the apparatus valve was opened at 03:50 JST on 5 March 2016 (Figure 8). Although the valve was closed between 28 February and 5 March, both temperature sensors recorded some positive excursions during that period, probably caused by a warm water mass transported from nearby vents by the bottom tidal current (Crone et al., 2005; Kinoshita et al., 1998; Tivey et al., 2002).

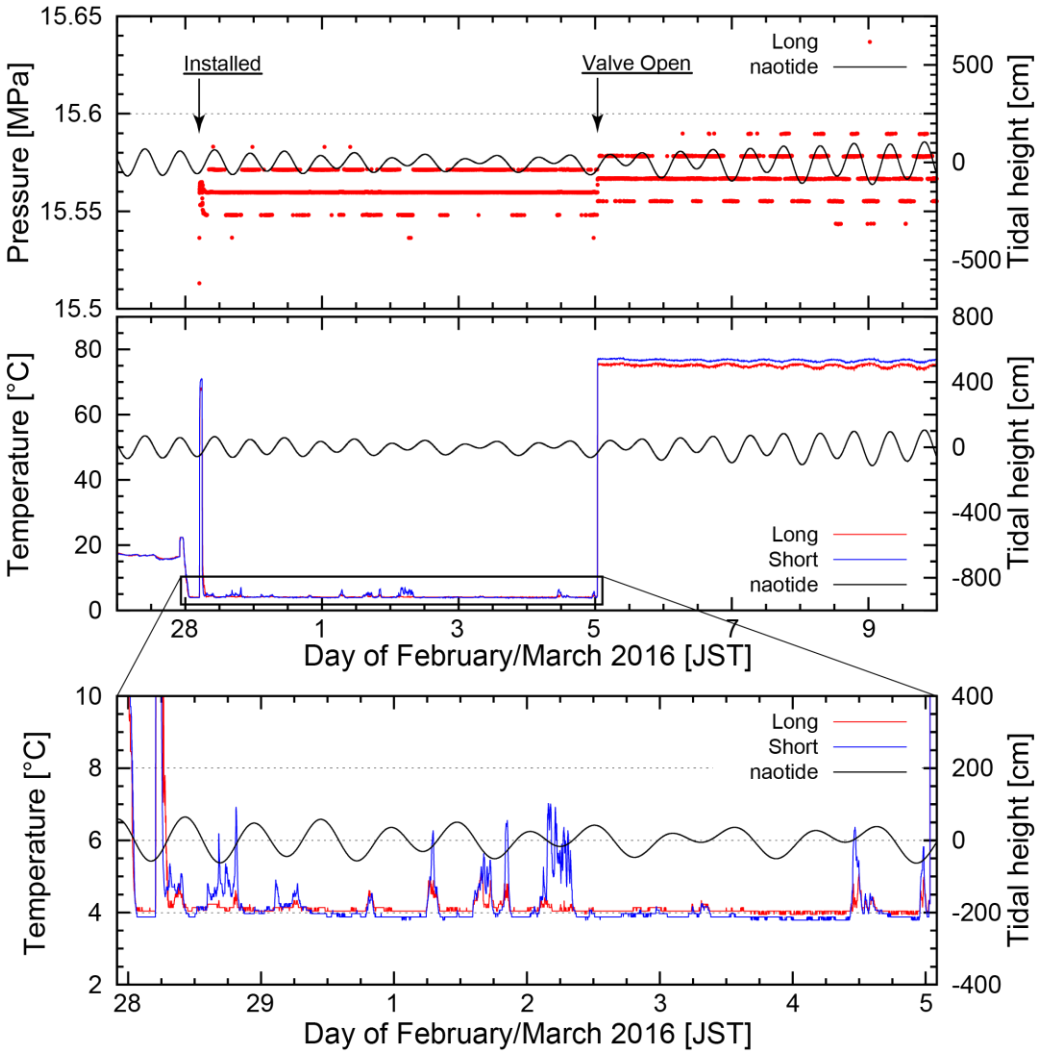

Figure 8. Pressure and temperature changes at the time of deployment. The apparatus was lowered to the seafloor and installed at the top of the casing on 28 February 2016. The valve was opened for long-term monitoring on 5 March 2016, at which time the pressure jumped by 7 kPa and the temperature jumped by ~70 °C. The bottom panel shows the temperature record at the seafloor. While on the seafloor, both sensors recorded some positive excursions, probably caused by a warm water mass transported by the bottom tidal current. The tidal variation started right after the installation, supporting the inference that it originated from the hydrothermal venting.

Immediately after the valve was opened, the temperatures recorded by both the long and short probes increased to 75–76 °C, and an abrupt increase in pressure of 7 kPa was observed. Also, both temperature (±0.3 °C) and pressure (±5 kPa) began to exhibit tidally modulated oscillations.

The pressure jump can be partly attributed to dynamic pressure caused by the hydrothermal venting at ~70 L/min. However, venting can explain an increase of only 100–200 Pa, estimated using Bernoulli's principle, which is much smaller than the observed pressure change. We suggest that there was a slight overpressure of ~7 kPa in the venting fluid.

Tidal modulation of temperature started right after the valve was opened; this fact supports the inference that the variation originates from the hydrothermal venting. Tidal modulation of pressure appeared to remain unchanged across the valve operation; although the data resolution is insufficient for a definitive conclusion, this fact suggests that the pressure variation within the apparatus was basically controlled by the ocean tide.

3.4. Excursions Related to Nearby Drilling

Between 30 November and 1 December 2016, both long and short probe temperatures suddenly dropped to the seawater value, then recovered by 3 December (Figure 3). This temperature drop coincides with a drilling operation for installation of another Kuroko ore-cultivation apparatus in Hole 9017A, only ~13 m ENE of Hole 9017B (Figure 1c). We infer that seawater artificially injected into Hole 9017A during the drilling operation reached Hole C9017B almost instantly, causing the temperature of the fluid discharged from the cultivation cell at Hole C9017B to decrease. The quick return to the temperature by 3 December suggests that the

420 influence of the artificially injected seawater on the subseafloor hydrothermal reservoir was
421 limited.

422

423 **4. Tidal Response Models**

424 In Section 3.2.2, we showed that the amplitude of the tidally modulated temperature
425 fluctuation gradually increased from ±0.4 °C to ±4 °C in synchrony with the decrease in the
426 temperature of the hydrothermal effluent from 76 °C to ~40 °C during Periods 2 and 3. Figure 9
427 shows the relationship between the average temperature and the M2 tidal amplitude, from which
428 the amplitude of the M2 component (12.4-h period) was calculated using a fast Fourier transform
429 (FFT). We also showed that the temperature within the Kuroko ore-cultivation apparatus was
430 constantly modulated by tidal processes with a phase lag of 150°.

431 Here, we discuss possible mechanisms for these variations in temperature and M2
432 amplitude. The gradual temperature decrease is probably attributable to a decrease in fluid flow
433 velocity through the apparatus. Although the flow velocity was not measured, this decrease is
434 supported by visual observations (Figure 4) showing a marked decrease in venting from the
435 exhaust pipes just before recovery of the apparatus (see Section 3.1). The decrease in flow might
436 have been caused by either a decay in thermal energy in the apparatus (natural origin) or
437 clogging of the apparatus (e.g., within the bottom inflow or top vent pipes). We visually
438 observed shimmering around the base platform, indicating that hydrothermal activity continued
439 below the seafloor (Section 3.1). Hydrological properties and the dimensions of the hydrothermal
440 reservoir affect the response (e.g., phase) to tidal loading, as described by Jupp and Schultz
441 (2004) and Barrayre et al. (2014). Because the phase lag remained stable at around 150°,

hydrological properties around the C9017B drill site remained stable during the observation period, even during the temperature decreases in Periods 2 and 3 (Figures 3, 9). Thus, we infer that clogging within the apparatus is more likely to be the cause of the flow decay.

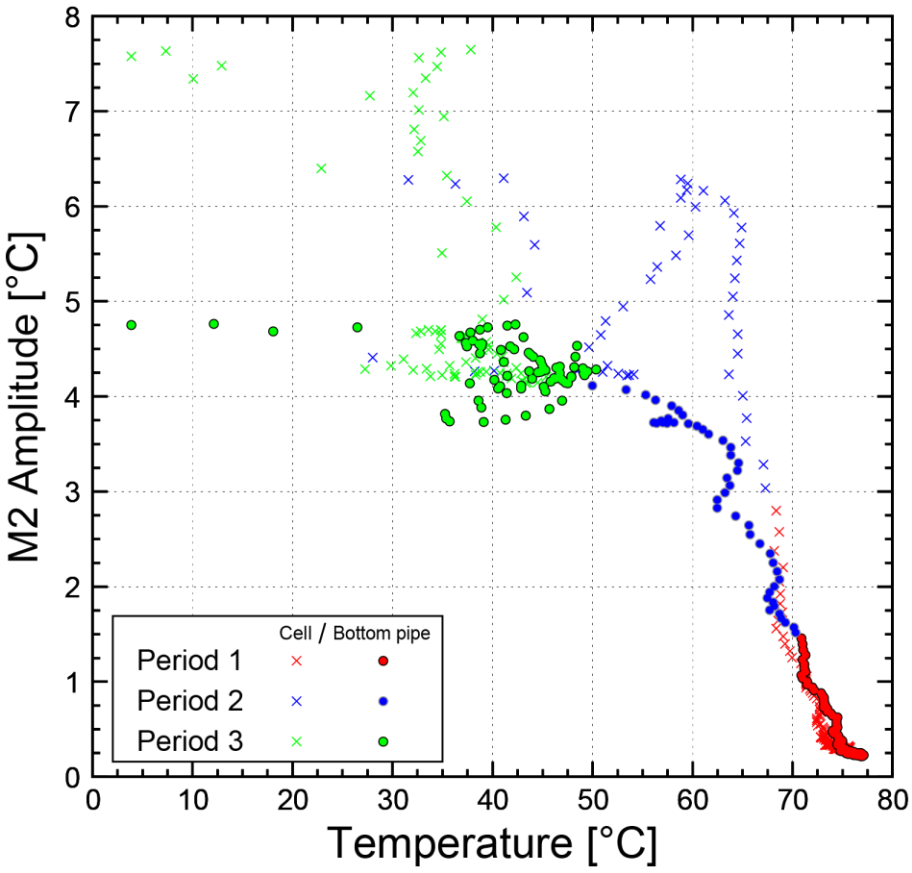

Figure 9. Correlation between temperature and the tidal variation amplitude. Cell: long-probe sensor in the cultivation cell. Bottom pipe: short-probe sensor in the bottom inflow pipe. The sampling interval was interpolated to 1 min. The M2 amplitude was calculated by FFT for a 14-day window, which was shifted by 1 day for each data point.

453 In Section 4.1, we show by a simple thermal conduction model that a decrease in flow
454 velocity through the Kuroko ore-cultivation apparatus can increase the amplitude of temperature
455 tidal modulation. In Section 4.2, we propose a plausible mechanism for the phase lag using a
456 combination of poroelastic and thermal modeling. We realize that it would be better to analyze
457 all phenomena (i.e., the gradual temperature decreases and the gradual increase in temperature
458 tidal amplitude, and the constant phase lag between temperature and pressure) simultaneously.
459 However, the flow during Period 1 (~60 cm/s) would have been mostly adiabatic and its
460 modeling requires different fluid dynamics. We leave such modeling to a later analysis and treat
461 each phenomenon separately here, using a steady-state model to estimate conductive cooling and
462 a time-dependent poroelastic/thermal model to simulate the temperature response to tidal
463 modulation.

464

465 **4.1. Conductive Cooling and Gradual Variation**

466 We assume here that the flow velocity through the Kuroko ore-cultivation apparatus
467 decreased gradually during Periods 2 and 3. We present a plausible scenario for what was
468 measured by the *P*/*T* sensors during the monitoring interval: First, clogging inside the apparatus
469 significantly depressed the inflow; second, the temperature inside the apparatus decreased as a
470 result of effective conductive cooling by the ambient seawater; and third, efficient cooling led to
471 an increase in the amplitude of tidal temperature variation.

472 To evaluate this scenario, we carried out numerical calculations of conductive cooling
473 through the apparatus inflow pipe above the seafloor. For simplicity, we assumed a steady state
474 with a constant flow rate within the pipe and a constant fluid temperature (76 °C) (Figure 10a).
475 This assumption is valid for the M2 (semi-diurnal) tide because its typical time constant (a few

476 hours) is sufficiently long compared that for thermal diffusion through the 2-inch ID bottom pipe
477 of the apparatus (~1,000 s).

478

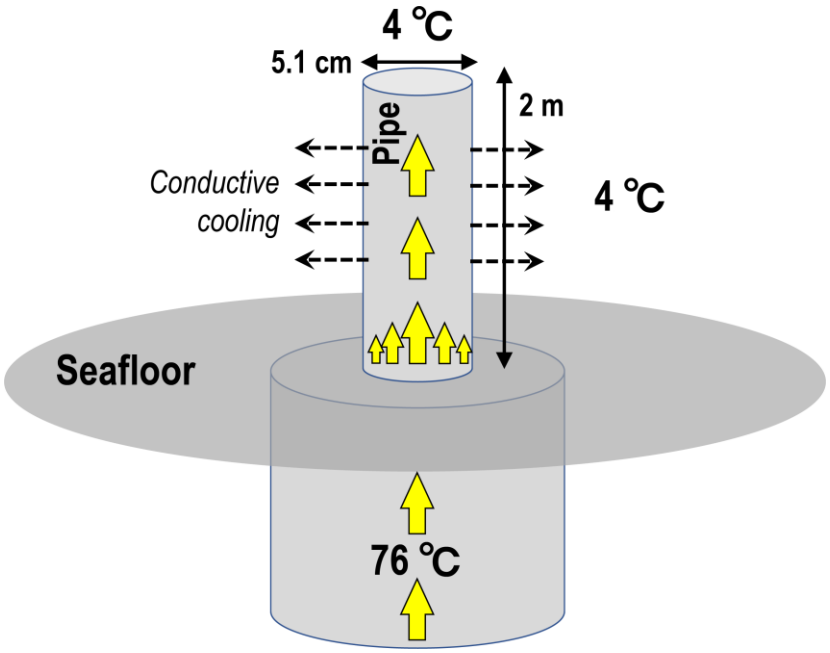

479

480 **Figure 10.** Settings and parameters of the conductive cooling numerical model.

481
482
483 **Table 3**. List of the observed/estimated properties for conductive cooling model
484

Property	Period 1		Period 3		Comments
	Obs.	Model	Obs.	Model	
Average temperature	76 ℃	-	40 ℃	-	
Tidal amplitude of temperature ΔT	~0.4 ℃	20 m℃ (z=1 m) 10 m℃ (z=0.5 m)	4~6 ℃	1.3 ℃ (z=1 m) 0.9 ℃ (z=0.5 m)	
Flow rate V	~60 cm/s	-	no data	~2 mm/s 2~3 mm/s	Analytical solution from eq(1) Numerical solution for T=40 ℃
Tidal amplitude of flow rate ΔV	~3 cm/s	-	no data	0.2~0.25 mm/s ~1 mm/s	Proportional allotment Numerical solution for dT=4 ℃

485
486

487

488 For the numerical simulation, we used the commercial COMSOL multiphysics software
489 package for the finite element method calculation and steady-state 2-D cylindrical coordinates.

Figure 10 and Table 3 show the model configuration and representative parameter values. Because cooling by ambient seawater occurs primarily in the bottom pipe, we conducted the simulation for a 2-inch diameter pipe extending 2 m above the seafloor. The temperature was set to 4 °C at the side and top boundaries of the pipe and to 76 °C at the bottom boundary, at the level of the seafloor. Flow velocity (V) in the center of the pipe was set to a constant value, independent of the longitudinal position in the pipe. The radial distribution of V followed a Poiseuille flow model assuming a laminar flow regime. We tested 14 different values of V (0.001–0.6 m/s) to cover the range of observed velocities at the beginning. To simulate the effect of tidal variation, we tested 16 velocity fluctuation values (dV = 0.0001–0.05 m/s) for each value of V, where ($V + dV$) was provided as the input to the simulation. Accordingly, 224 calculations of temperature (T) and its amplitude (dT) were carried out using every possible combination of V and dV.

Figure 11 shows the calculated temperature distributions resulting from conductive cooling during Periods 1 and 3. The flow velocity measured at the beginning of the study period was used for the value of V during Period 1 (V = 60 cm/s; see Section 3.2.3). For the value of V during Period 3 (4 mm/s), we selected the value that best fit the observed temperature (~40 °C) and its tidal variation amplitude ($dT \approx 4$ °C), as explained below.

In Figure 12a, calculated temperatures are plotted against various flow velocities at 50 cm above the seafloor and at three different horizontal (radial) distances r relative to the center position (r = 0 cm). A significant decrease in temperature as well as an increase in dT/dV (temperature sensitivity to velocity change) is clearly seen for velocities slower than 0.01 m/s (Figure 12a). The increase in dT/dV with average flow velocity indicates that temperature is more sensitive to tidal variations at slower flow velocities.

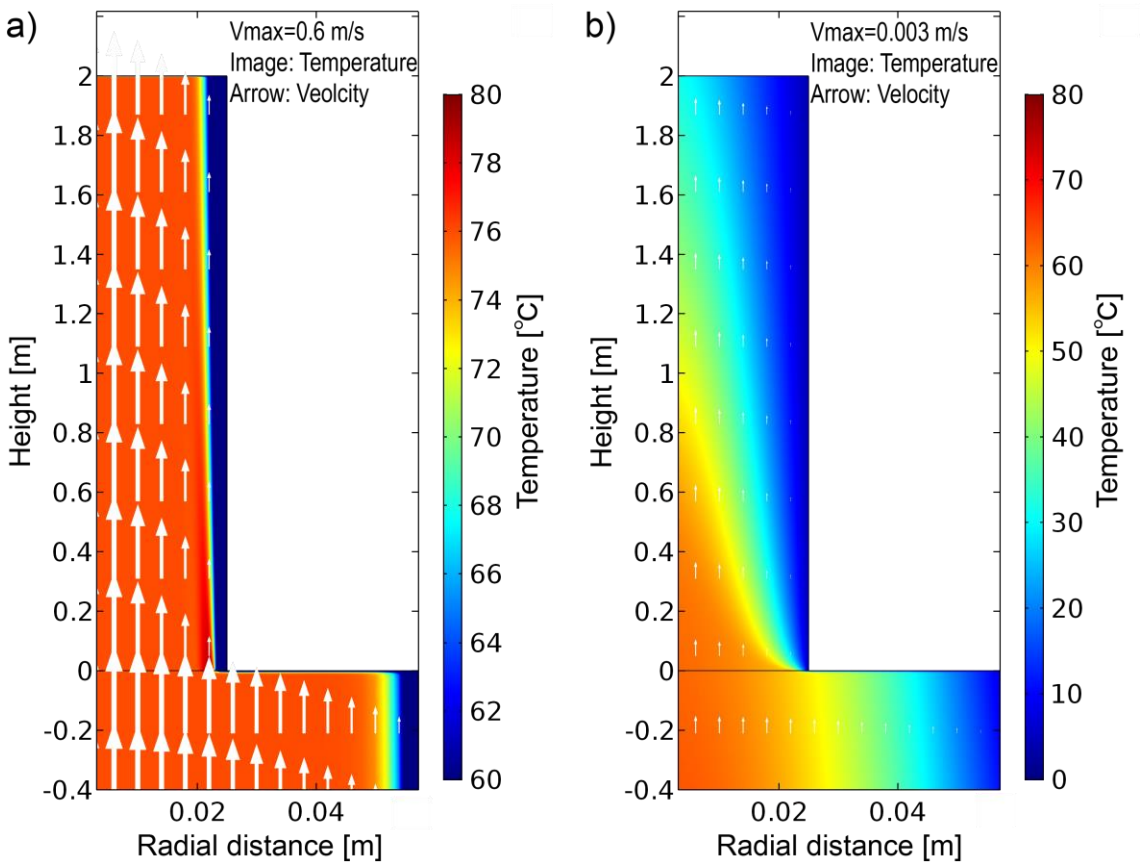

Figure 11. Results of the conductive cooling model calculations in a pipe simulating a simplified Kuroko ore-cultivation apparatus. (a) Period 1 (V = 60 cm/s), (b) Period 3 (V = 3 mm/s). Note the difference in the color scale: 60–80 °C in (a) but 0–80 °C in (b). White arrows are proportional to flow velocity.

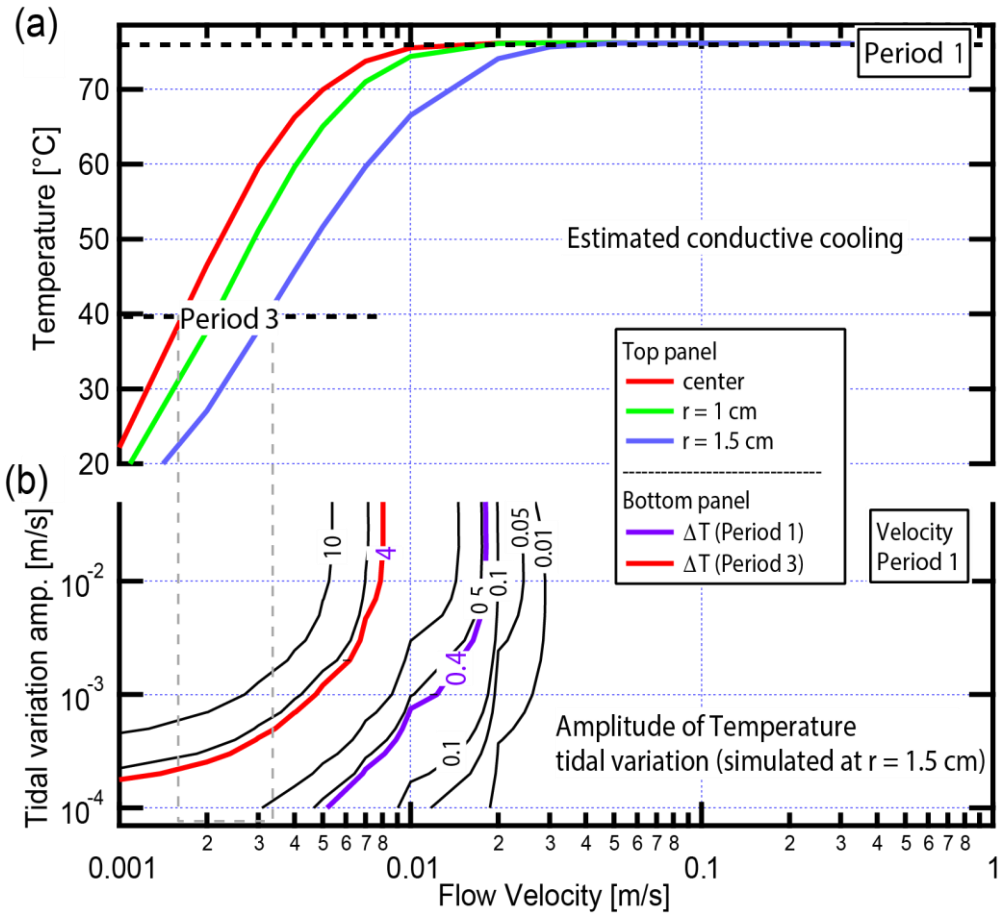

Figure 12. (a) Predicted temperature at 50 cm above the seafloor in the 2-inch pipe at various flow velocities. The "Period 1" marker shows the observed velocity (~60 cm/s) and temperature (76 °C) during Period 1. The "Period 3: marker shows the observed temperature (40 °C) and the predicted velocity range between the center and a radius (*r*) of ~1.5 cm. (b) Predicted amplitude of the temperature variation (*dT*; contours, °C) plotted against average flow velocity (*V*, *x*-axis) and tidal variation amplitude (*dV*; vertical) simulated at *r* =1.5 cm. The thick red and blue contours correspond to the observed temperature variation during Period 1 (0.4 °C) and Period 3 (4 °C), respectively. Vertical broken lines connecting (a) and (b) show the predicted velocity range during Period 3. The corresponding velocity amplitude is several millimeters per second.

536 To clarify this velocity dependence, Figure 12b shows contours of the amplitude of the
537 temperature tidal variation (dT) versus the central velocity (V) and the amplitude of the velocity
538 tidal variation (dV). During Period 1 ($V \approx 60$ cm/s, $dV \approx 3$ cm/s), $dT < 1$ mK, much less than the
539 observed variation (±0.4 °C). This result indicates that not only the velocity but also the
540 temperature of the hydrothermal discharge fluid itself varied, even before entering the bottom
541 inflow pipe.

542 During Period 3, the temperature in the apparatus was ~40 °C; thus, a reduction of the
543 flow velocity in the pipe to 1.5–3.2 mm/s can be inferred from Figure 12a. Then, by referring to
544 Figure 12b, the amplitude of velocity variation dV can be estimated as 0.2–0.5 mm/s based on
545 the observed temperature variation dT (red contour, ±4 °C). Although velocity was not directly
546 observed during Period 3, the ratio of its fluctuation amplitude to the average flow velocity
547 (dV/V) is ~13%, of the same order of magnitude as that in the beginning of the study period
548 (~5%). The larger amplitude of temperature variation during Period 3 is well explained by
549 enhanced conductive cooling, caused by the reduced average flow velocity in the pipe.

550 The notable velocity reduction during Periods 2 and 3 probably allowed ambient seawater
551 to enter the cultivation cell via the outlet. This inference is supported by the observation of
552 negative temperature excursions only during low-temperature (high-tide) periods, when the
553 upward velocity was at a minimum (or even downward). We suggest that the pipes became
554 completely clogged at low-temperature moments, which allowed seawater ingress. With the
555 return to “low tide”, the flow path reopened and smooth throughflow resumed.
556

4.2. Poroelastic Response to Ocean Tides

Here we discuss the cause of the phase lag of the temperature variations within the Kuroko ore-cultivation apparatus. Several possible mechanisms might modulate temperature. First, a tidally forced bottom current might carry warm fluid discharged into the water column downstream (Crone et al., 2005; Kinoshita et al., 1998; Tivey et al., 2002). However, such a disturbance would cause the variation envelope to be different and more irregular than a sinusoidal envelope (see Section 3.3 and Figure 8). Moreover, the sinusoidal variation started only after the valve of the apparatus was opened on 5 March 2016. Thus, we reject this possible mechanism.

Second, a dynamic pressure change caused by fluid movement within the pipe might have an effect. The dynamic pressure change is simply calculated from the velocity (V = 60 cm/s) and its variation amplitude (dV = 3 cm/s). However, the calculated pressure change in response to the fluid movement is negligibly small at only 5 Pa. Thus, we also reject this possibility and consider the pressure variation in the system to be hydrostatic.

In Section 4.1, we showed that the temperature variation during Period 1 was much larger than that produced by conductive cooling alone. Also, the temperature variations recorded by the two sensors (at the top of the cultivation cell and within the bottom inflow pipe) were almost identical in both amplitude and phase (Figure 5). These findings strongly suggest that a major portion of the temperature oscillation originated in the subseafloor hydrothermal reservoir beneath the apparatus. Thus, we assume that the temperature oscillation originated from the subseafloor poroelastic response to tidal loading.

According to Barreyre et al. (2014), poroelastic models predict tidal modulation of discharge velocity and temperature via the propagation of pressure transients into the shallow

crust (e.g., Crone & Wilcock, 2005; Jupp & Schultz, 2004; Wang & Davis, 1996). Alternatively, cracks in the subseafloor hydrothermal reservoir can be deformed by tidal stress variations (e.g., Crampin & Chastin, 2003). Because water is more compressible than solids, tides can cause underground cracks to open and close, thereby causing changes in permeability. Such a permeability change would affect the poroelastic response. LWD image at Hole C9017A indicated a conductive zone at 24-42 mbsf (Kumagai et al., 2017). Although this interval may be the high permeability zone, we do not consider it in the current analysis because relevant knowledge on subseafloor hydrological structure is lacking at this time.

4.3. Numerical Modeling of the Tidal Modulation

The goal of our numerical simulation was to find the model that can best explain the 150° phase lag of the temperature variation of the fluid before it enters the Kuroko ore-cultivation apparatus. The additional phase shift occurring within the apparatus was negligible, because temperature variations in the cultivation cell (long probe) and the bottom inflow pipe (short probe) sensors were almost identical in both amplitude and phase (Figure 5).

We again used the COMSOL multiphysics package for finite element method time-dependent modeling in a 2-D cylindrical coordinate system (Figure 13). Multiphysics components include solid mechanics, Darcy's flow, and heat transfer in porous media. We set the borehole depth to 20 m and its diameter to 30 cm with high permeability (10^{-10} m^2) and a low Young's modulus (1 GPa) (see Table 4 for detailed parameter settings). We allowed hydrothermal circulation and pressure-driven flow only in a region within a 50 m radius of the borehole extending to a depth of 50 mbsf where the Young's modulus was set to 5 GPa. The

permeability was set to exponentially decay with increasing depth, and its initial value was varied between 10^{-10} m^2 and 10^{-16} m^2. Temperature on the seafloor was set at 4 °C, and the side boundary was set to adiabatic (i.e., no horizontal heat transfer was allowed). The center bottom temperature was fixed at 304 °C and it was allowed to gradually decrease toward the periphery. Tidal loading at the seafloor was given as a sinusoidal pressure variation with an amplitude of ±10 kPa and a period of 12.4 h (M2 tide).

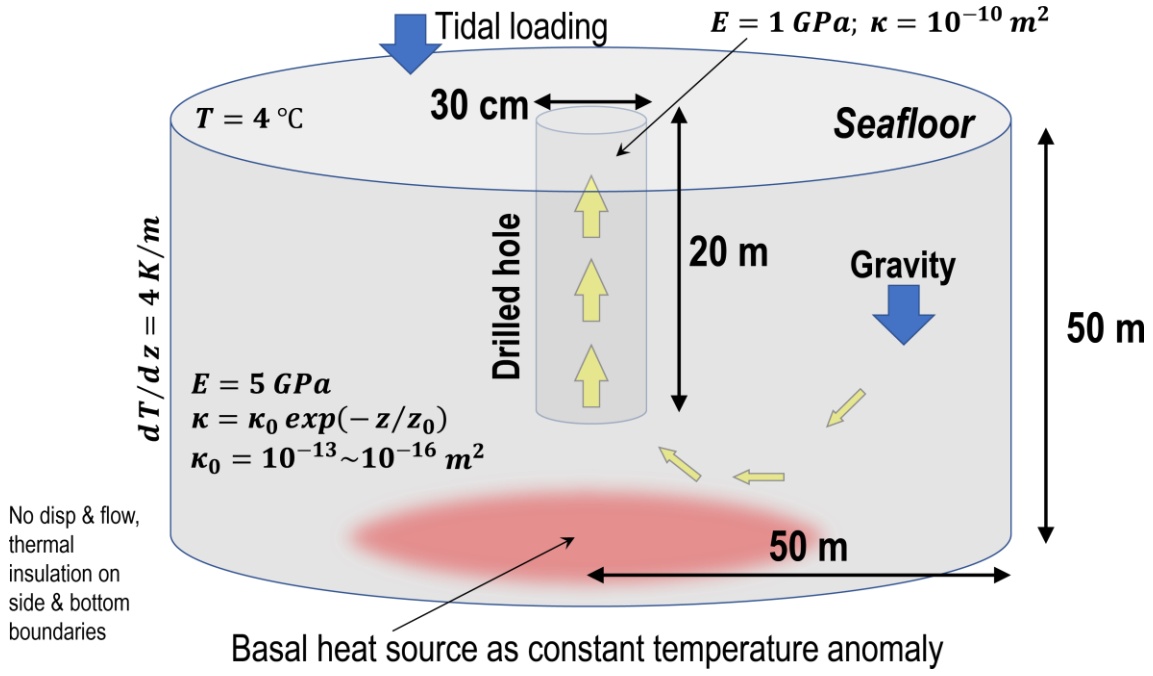

Figure 13. Numerical model settings for the poroelastic and thermal response to the tidal loading.

Table 4. Model parameters for calculating poroelastic response to ocean tide.

Description	Domain 1 - sediment	Domain 2 - drillhole
Dimension		
Radial (r)	0 - 50 [m]	0 - 15 [cm]
Vertical (z) *positive downward	0 - 50 [m]	0 - 20 [m]
Elastic propertyies (Sold mechanics)		
Young's Modulus	5 [GPa]	1 [GPa]
Poisson's ratio	0.4	0.4
Loading efficiency	0.7	0.7
Density (in solid mechanics)	2000 [kg m^{-3}]	
Surface load (=surface pressure)	$10\ [\mathrm{kPa}]\ \sin\left(\frac{2\pi t}{T_{M2}}\right)$	
Hydrological properties (Darcy's law)		
Dynamic viscosity	$0.38[\mathrm{Pa}\cdot\mathrm{s}]\exp(-0.02\mathrm{T}[\mathrm{K}])$	
Compressibility	1/5 [1/GPa]	1 [1/GPa]
porosity on the seafloor (ϕ_0)	0.7	0.7
Fractional Porosity	$\phi_0 \exp\left(\frac{-z}{500[\mathrm{m}]}\right)$	ϕ_0
Permeability on the seafloor (κ_0)	10^{-13} ~10^{-16} [m^2]	10^{-10} [m^2]
Permeability	$\kappa_0 * 10^{\left(\frac{-z}{50[\mathrm{m}]}\right)}$ [m^2]	10^{-10} [m^2]
Heat transfer in porous media		
Water density on the seafloor (ρ_0)	1030 [kg m^{-3}]	
Thermal expansion coefficient of water (α)	10^{-4} [1/K]	
Fluid density	$\rho_0 * (1 - \alpha(T - T_0))$	
Density of solid grain (ρ_s)	2700 [kg m^{-3}]	
Fluid thermal conductivity	0.6 [W m^{-1} K^{-1}]	
Thermal conductivity of solid material	2 [W m^{-1} K^{-1}]	
Thermal conductivity of formation	Estimated by geometrical mean model	
Fluid heat capacity	4200 [J/K/kg]	
Ratio of specific heat	1	
Specific heat of solid matrix	1800 [J/kg/K]	
Temperature on the seafloor (T_0)	4 [℃]	
Vertical thermal gradient (G)	4 [K/m]	
Temperature at the bottom boundary (gp=gaussian function)	$T_0 + 300 * gp\left(\frac{r}{50[m]}\right)$ [℃]	
Initial temperature	T_0 + (-z)*G	

617

618

619

620 First, the background hydrothermal circulation was calculated until it equilibrated. Then,
621 using this result as the initial condition, tidal loading was applied at the seafloor and the
622 temperature response to the tidal loading was calculated for 20 h.

623 Figure 14 shows the calculated temperatures at the center of the pipe (r = 0) and at 5 m
624 below the seafloor for four surface permeabilities. As demonstrated previously (e.g., Crone &
625 Wilcock, 2005), the temperature phase lag depends largely on the subseafloor permeability,
626 increasing as permeability increases. From this calculation, we infer that a high permeability (k_0
627 > 10^{-13} m^2) is required to account for the observed phase lag. We do not discuss the amplitude of
628 the temperature variation here because the model does not fully reflect the actual site structure.
629 However, the observed amplitude for $k_0 = 10^{-13}$ m^2 is ±0.5 °C, consistent with the observations
630 (0.4 °C).

631 Jupp and Schultz (2004) showed that the temperature phase also depends on the tidal skin
632 depth, that is, the depth over which pore pressure signals can diffuse during one tidal cycle. The
633 skin depth depends on permeability, so we can infer that the dimensions of the hydrothermal
634 reservoir (approximated as the permeable region) remained unchanged throughout the
635 observation period. However, further observations and analysis are needed to resolve both the
636 hydrological properties and the spatiotemporal scale of the reservoir.

637

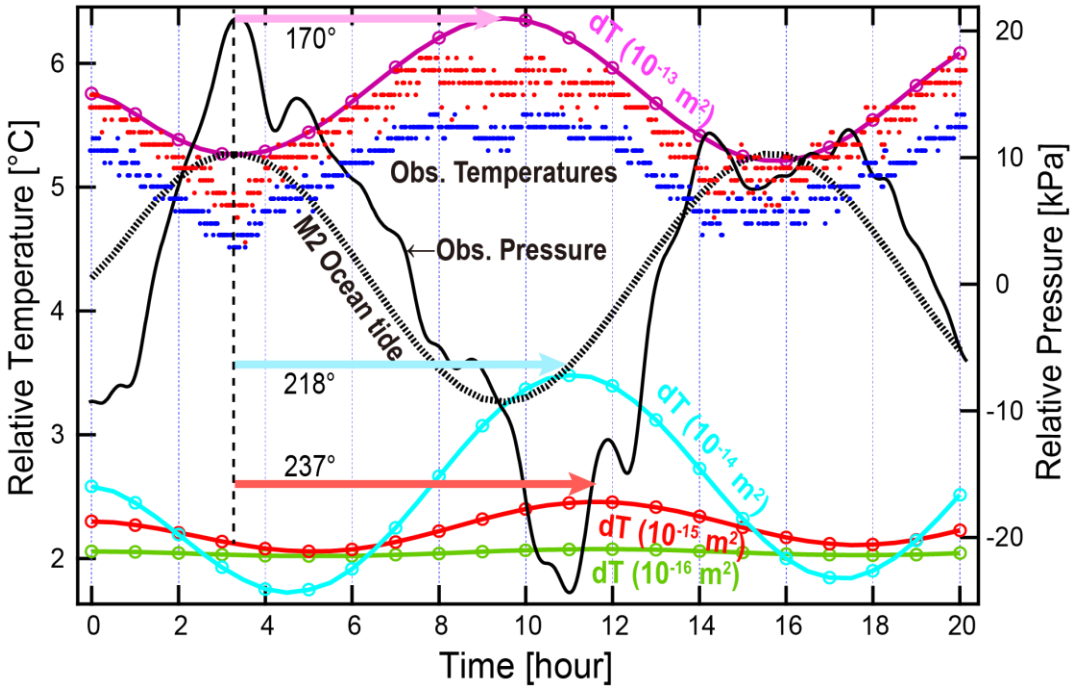

Figure 14. Simulated temperature phase lags for four different permeabilities (colored solid curves with circles; left axis) relative to the M2 ocean tide pressure (black dashed curve; right axis). Phase lag values are shown by colored arrows. The solid black curve shows the observed pressure smoothed in a 200-min window; the peak location has been shifted to match that of the simulated ocean tide. The dotted curves show observed temperatures in the cell (red) and in the 2-inch bottom inflow pipe (blue); they are horizontally shifted by the same amount as the observed pressure, and vertically shifted to fit within the figure.

5. Conclusions

Temperature observations carried out over 10 months within a Kuroko ore-cultivation apparatus provided critical information about the Noho hydrothermal system in the mid-Okinawa Trough, SW Japan:

-Temperature and pressure in the apparatus started fluctuating in accordance with tidal frequency immediately after installation, indicating that the fluctuation originated in the subseafloor hydrothermal reservoir.

-The initial temperature was 75–76 °C with a tidal modulation amplitude of ~0.3 °C. Four months later, the tidally modulated amplitude of temperature fluctuations gradually increased to ±4 °C synchronous with a decrease in the average temperature to ~40 °C. The phase lag remained unchanged.

-The phase of the temperature fluctuation lagged that of the pressure fluctuation by ~150°, and the lag remained unchanged throughout the observation period.

A numerical conductive cooling model showed that the gradual change in temperature could be attributed to a gradual decrease in inflow to the apparatus that promoted conductive cooling through the pipe. This probably indicates that a significant volume of the hot hydrothermal fluid drained out as a result of drilling, implying that the reservoir size became smaller. The temperature phase lag is interpreted as a poroelastic response of the hydrothermal reservoir to ocean tides. Higher permeability in the reservoir ($\sim 10^{-13}$ m^2) than in the surrounding formation is required to generate the 150° phase lag.

Acknowledgments

This work was supported by the Council for Science, Technology and Innovation (CSTI) through its Cross-ministerial Strategic Innovation Promotion Program (SIP) "Next-generation technology for ocean resources exploration". We acknowledge the crew and drillers of D/V *Chikyu*, the crew and diving teams of R/V *Kairei* and ROV *Kaiko MK-IV*, and the science parties aboard cruises CK16-01 (D/V *Chikyu* Exp. 908), CK16-05 (D/V *Chikyu* Exp. 909), KR16-17, and KR18-02C. Special gratitude is owed to Yuka Masaki of Cosmos Shoji Co., Ltd, as well as to Hidenori Kumagai and Lena Maeda of JAMSTEC for the success of these long-term monitoring and in situ experiments. The figures in this study were created using the GMT software package (Wessel et al., 2013). The data used in this study are available at Data and Sample Research System for Whole Cruise Information (DARWIN; http://www.godac.jamstec.go.jp/darwin/e) of JAMSTEC.

References

Arai, R., Kodaira, S., Kaiho, Y., Takahashi, T., Miura, S., & Kaneda, Y. (2017), Crustal structure of the southern Okinawa Trough: Symmetrical rifting, submarine volcano, and potential mantle accretion in the continental back-arc basin, *J. Geophys. Res. Solid Earth*, *122*, 622–641. https://doi.org/10.1002/2016JB013448

Barreyre, T., Escartín, J., Sohn, R. A., Cannat, M., Ballu, V., & Crawford, W. C. (2014), Temporal variability and tidal modulation of hydrothermal exit-fluid temperatures at the Lucky Strike deepsea vent field, Mid-Atlantic Ridge, *J. Geophys. Res. Solid Earth*, *119*, 2543–2566. https://doi.org/10.1002/2013JB010478

691 Barreyre, T., & Sohn R. A. (2016), Poroelastic response of mid-ocean ridge hydrothermal
692 systems to ocean tidal loading: Implications for shallow permeability structure, *Geophys.*
693 *Res. Lett.*, *43*, 1660–1668. https://doi.org/10.1002/2015GL066479

694 Crampin, S., & Chastin, S. (2003), A review of shear wave splitting in the crack-critical crust,
695 *Geophys. J. Int.*, *155*, 221–240. https://doi.org/10.1046/j.1365-246X.2003.02037.x

696 Crone, T. J., & Wilcock, W. S. D. (2005), Modeling the effects of tidal loading on mid-ocean
697 ridge hydrothermal systems, *Geochem. Geophys. Geosyst.*, *6*, Q07001.
698 https://doi.org/10.1029/2004GC000905

699 Glasby, G. P., & Notsu, K. (2003), Submarine hydrothermal mineralization in the Okinawa
700 Trough, SW of Japan: an overview. *Ore Geol. Rev.*, *23*(3-4), 299–339.
701 https://doi.org/10.1016/j.oregeorev.2003.07.001

702 Halbach, P., Nakamura, K.-I., Wahsner, M., Lange, J., Sakai, H., Käselitz, L., et al. (1989),
703 Probable modern analogue of Kuroko-type massive sulphide deposits in the Okinawa
704 Trough back-arc basin. *Nature*, *338*, 496–499. https://doi.org/10.1038/338496a0

705 Ishibashi, J.-i., Ikegami, F., Tsuji, T., & Urabe, T. (2015), Hydrothermal Activity in the Okinawa
706 Trough Back-Arc Basin: Geological Background and Hydrothermal Mineralization. In:
707 Ishibashi, J., Okino, K., Sunamura, M. (eds) Subseafloor Biosphere Linked to
708 Hydrothermal Systems (pp. 337–359), Springer, Tokyo. https://doi.org/10.1007/978-4-
709 431-54865-2_27

710 Ishibashi, J.-i., & Urabe, T. (1995), Hydrothermal Activity Related to Arc-Backarc Magmatism
711 in the Western Pacific. In: Taylor B. (eds) Backarc Basins (pp. 451–495), Springer,
712 Boston, MA. https://doi.org/10.1007/978-1-4615-1843-3_13

713 Jupp, T. E., & Schultz A. (2004), A poroelastic model for the tidal modulation of seafloor
714 hydrothermal systems, *J. Geophys. Res. Solid Earth*, *109*, B03105.
715 https://doi.org/doi:10.1029/2003JB002583

716 Kasaya, T., Kaneko, J., & Iwamoto, H. (2020), Observation and confirmation based on survey
717 protocol for seafloor massive sulfide deposits using acoustic survey technique and self-
718 potential surveys [in Japanese with English abstract], BUTSURI-TANSA, 73, 33–41.
719 https://doi.org/10.3124/segj.73.42

720 Kawagucci, S., Miyazaki, J., Nakajima, R., Nozaki, T., Takaya, Y., Kato, Y., et al. (2013), Post-
721 drilling changes in fluid discharge pattern, mineral deposition, and fluid chemistry in the
722 Iheya North hydrothermal field, Okinawa Trough, *Geochem. Geophys. Geosyst.*, *14*(11),
723 4774–4790. https://doi.org/10.1002/2013GC004895

724 Kawagucci, S., Shirai, K., Lan, T. F., Takahata, N., Tsunogai, U., Sano, Y., & Gamo, T. (2010),
725 Gas geochemical characteristics of hydrothermal plumes at the HAKUREI and JADE
726 vent sites, the Izena Cauldron, Okinawa Trough, *Geochem. J.*, *44*(6), 507–518.
727 https://doi.org/10.2343/geochemj.1.0100

728 Kimura, M. (1985), Back-arc rifting in the Okinawa Trough, *Mar. Pet. Geol.*, *2*(3), 222–240.
729 https://doi.org/10.1016/0264-8172(85)90012-1

730 Kimura, M., Uyeda, S., Kato, Y., Tanaka, T., Yamano, M., Gamo, T., et al. (1988), Active
731 hydrothermal mounds in the Okinawa Trough backarc basin, Japan, *Tectonophysics*,
732 *145*(3-4), 319-324. https://doi.org/10.1016/0040-1951(88)90203-X

733 Kinoshita, M., Von Herzen, R. P., Matsubayashi, O., & Fujioka, K. (1998), Erratum to 'Tidally-
734 driven effluent detected by long-term temperature monitoring at the TAG hydrothermal

735 mound, Mid-Atlantic Ridge [Phys. Earth Planet. Int. 108(1998) 143-154], *Phys. Earth*
736 *Planet. Int.*, *109*, 201-212. https://doi.org/10.1016/S0031-9201(98)00129-0

737 Kinoshita, M., & Yamano, M. (1997), Hydrothermal regime and constraints on reservoir depth
738 of the Jade site in the Mid-Okinawa Trough inferred from heat flow measurements, *J.*
739 *Geophys. Res. Solid Earth*, *102*(B2), 3183-3194. https://doi.org/10.1029/96JB03556

740 Kinoshita, M., Yamano, M., Post, J., & Halbach, P. (1990), Heat Flow Measurements in the
741 Southern and Middle Okinawa Trough on R/V Sonne in 1988, *Bull. Earthquake Res. Inst.*
742 *Univ. Tokyo*, *65*, 571-588.

743 Komori, S., Masaki, Y., Tanikawa, W., Torimoto, J., Ohta, Y., Makio, M., et al. (2017), Depth
744 profiles of resistivity and spectral IP for active modern submarine hydrothermal deposits:
745 a case study from the Iheya North Knoll and the Iheya Minor Ridge in Okinawa Trough,
746 Japan, *Earth Planets Space*, *69*, 114. https://doi.org/10.1186/s40623-017-0691-6

747 Kumagai, H., Nozaki, T., Ishibashi, J.-i., Maeda, L., & CK16-01 on-board member (2017),
748 *Cruise report SIP-HOT II "Explorer" (SIP–Hydrothermal deposit in Okinawa Trough)*
749 *CK16-01 (Exp. 908)*, Yokosuka, Japan: JAMSTEC.

750 Larson, B. I., Olson, E. J., & Lilley, M. D. (2007), In situ measurement of dissolved chloride in
751 high temperature hydrothermal fluids, *Geochim. Cosmochim. Acta*, *71*, 2510–2523.
752 https://doi.org/10.1016/j.gca.2007.02.013

753 Lee, C. S., Shor Jr, G. G., Bibee, L. D., Lu, R. S., & Hilde, T. W. (1980), Okinawa Trough:
754 origin of a back-arc basin, *Mar. Geol.*, *35*(1-3), 219–241.

Letouzey, J., & Kimura, M. (1985), Okinawa Trough genesis: structure and evolution of a backarc basin developed in a continent, *Mar. Petrol. Geol.*, *2*(2), 111–130. https://doi.org/10.1016/0264-8172(85)90002-9

Letouzey, J., & Kimura, M. (1986), The Okinawa Trough: Genesis of a back-arc basin developing along a continental margin. *Tectonophysics*, *125*(1-3), 209-230. https://doi.org/10.1016/0040-1951(86)90015-6

Liu, B., Li, S. Z., Suo, Y. H., Li, G. X., Dai, L. M., Somerville, I. D., et al. (2016), The geological nature and geodynamics of the Okinawa Trough, Western Pacific. *Geol. J.*, *51*, 416–428. https://doi.org/10.1002/gj.2774

Masaki, Y., Kinoshita, M., Inagaki, F., Nakagawa, S., & Takai K. (2011), Possible kilometer-scale hydrothermal circulation within the Iheya-North field, mid-Okinawa Trough, as inferred from heat flow data, *JAMSTEC Rep. Res. Dev.*, *12*, 1-12. https://doi.org/10.5918/jamstecr.12.1

Masaki, Y., Nozaki, T., Saruhashi, T., Kyo, M., Sakurai, N., Yokoyama, T., Akiyama, K., Maeda, L., & Kumagai, H. (2017), Long-term sensor monitoring equipped with the Kuroko cultivation apparatus on the deep-sea artificial hydrothermal vent at the middle Okinawa Trough, 2017 GSA Cordilleran Section Meeting, Honolulu.

Matsumoto, K., Takanezawa, T., & Ooe, M. (2000), Ocean tide models developed by assimilating TOPEX/POSEIDON altimeter data into hydrodynamical model: A global model and a regional model around Japan, *J. Oceanography*, *56*, 567-581. https://doi.org/10.1023/A:1011157212596

776 Miyazaki, J., Makabe, A., Matsui, Y., Ebina, N., Tsutsumi, S., Ishibashi, J.-i., & et al. (2017),
777 WHATS-3: An Improved Flow-Through Multi-bottle Fluid Sampler for Deep-Sea
778 Geofluid Research, Front. Earth Sci., 5:45. https://doi.org/10.3389/feart.2017.00045

779 Nozaki, T. (2017), Long-term monitoring of hydrothermal fluid and in-situ mineral precipitation
780 experiment using a deep-sea artificial hydrothermal vent, 3rd Annual Asia-Pacific Deep
781 Sea Mining, Singapore.

782 Nozaki, T., Ishibashi, J.-i., Shimada, K., Nagase, T., Takaya, Y., Kato, Y., et al. (2016), Rapid
783 growth of mineral deposits at artificial seafloor hydrothermal vents, *Sci. Rep., 6*, 22163.
784 https://doi.org/10.1038/srep22163

785 Nozaki, T., Nagase, T., Takaya, Y., Yamasaki, T., Otake, T., Yonezu, K., et al. (2021a),
786 Subseafloor sulphide deposit formed by pumice replacement mineralisation, *Sci. Rep.*,
787 *11*, 8809. https://doi.org/10.1038/s41598-021-87050-z

788 Nozaki, T., Nagase, T., Torimoto, J., Takaya, Y., Ishibashi, J.-i., Shimada, K., et al. (2019), In-
789 situ mineral precipitation experiment by using a deep-sea artificial hydrothermal vent,
790 Goldschmidt 2019, Barcelona.

791 Nozaki, T., Nagase, T., Torimoto, J., Takaya, Y., Ishibashi, J.-i., Shimada, K., et al. (2021b),
792 Formation of highly Zn-enriched sulfide scale at a deep-sea artificial hydrothermal vent,
793 Iheya-North Knoll, Okinawa Trough, *Miner. Depos.*, *56*, 975–990.
794 https://doi.org/10.1007/s00126-020-01022-3

795 Nozaki, T., Nagase, T., Ushikubo, T., Shimizu, K., Ishibashi, J.-i., Shimada, K. & the D/V
796 Chikyu Expedition 909 Scientists (2021c), Microbial sulfate reduction plays an important

role at the initial stage of subseafloor sulfide mineralization, *Geology*, *49*(2), 222–227. https://doi.org/10.1130/G47943.1

Sakai, H., Gamo, T., Kim, E. S., Shitashima, K., Yanagisawa, F., Tsutsumi, M., et al. (1990), Unique chemistry of the hydrothermal solution in the mid-Okinawa Trough Backarc Basin, *Geophys. Res. Lett.*, *17*(12), 2133–2136. https://doi.org/10.1029/GL017i012p02133

Sawyer, A. H., Flemings, P., Elsworth, D. & Kinoshita, M. (2008), Response of submarine hydrologic monitoring instruments to formation pressure changes: Theory and application to Nankai advanced CORKs, *J. Geophys. Res. Solid Earth*, *113*, B01102. https://doi.org/10.1029/2007JB005132

Sibuet, J.-C., Deffontaines, B., Hsu, S.-K., Thareau, N., Le Formal, J.-P., Liu, C.-S., & ACT party (1998), Okinawa trough backarc basin: Early tectonic and magmatic evolution, *J. Geophys. Res.*, *103*(B12), 30245–30267. https://doi.org/10.1029/98JB01823

Sibuet, J.-C., Letouzey, J., Barbier, F., Charvet, J., Foucher, J.-P., Hilde, T. W. C., et al. (1987), Back Arc Extension in the Okinawa Trough, *J. Geophys. Res.*, *92*(B13), 14041–14063. https://doi.org/10.1029/JB092iB13p14041

Sohn, R. A. (2007a), Stochastic analysis of exit fluid temperature records from the active TAG hydrothermal mound (Mid-Atlantic Ridge, 26°N): 1. Modes of variability and implications for subsurface flow, *J. Geophys. Res. Solid Earth*, *112*, B07101. https://doi.org/10.1029/2006JB004435

Sohn, R. A. (2007b), Stochastic analysis of exit fluid temperature records from the active TAG hydrothermal mound (Mid-Atlantic Ridge, 26°N): 2. Hidden Markov models of flow

episodes, *J. Geophys. Res. Solid Earth*, *112*, B09102. https://doi.org/10.1029/2007JB004961

Takai, K., Mottl, M. J., Nielsen, S. H., & the Expedition 331 Scientists (2011), *Proc. IODP*, *331*, Integrated Ocean Drilling Program Management International, Inc., Tokyo. https://doi.org/10.2204/iodp.proc.331.2011

Takai, K., Mottl, M. J., Nielsen, S. H. H., & the IODP Expedition 331 Scientists (2012), IODP Expedition 331: Strong and expansive subseafloor hydrothermal activities in the Okinawa Trough, *Sci. Dril.*, *13*, 19–27. https://doi.org/10.2204/iodp.sd.13.03.2011

Tamura, Y., & Agnew, D. C. (2008), Baytap08 User's Manual, UC San Diego: Library – Scripps Digital Collection. Retrieved from https://escholarship.org/uc/item/4c27740c

Tivey, M. K., Bradley, A. M., Joyce, T. M., & Kadko D. (2002), Insights into tide-related variability at seafloor hydrothermal vents from time-series temperature measurements, *Earth Planet. Sci. Lett.*, *202*, 693–707. https://doi.org/10.1016/S0012-821X(02)00801-4

Wang, K., & Davis, E. E. (1996), Theory for the propagation of tidally induced pore pressure variations in layered subseafloor formations, *J. Geophys. Res. Solid Earth*, *101*(B5), 11483–11495. https://doi.org/10.1029/96JB00641

Wessel, P., Smith, W. H. F., Scharroo, R., Luis, J., & Wobbe, F. (2013), Generic Mapping Tools: Improved version released, EOS Trans. AGU, 94(45), 409–410. https://doi.org/10.1002/2013EO450001

Yamano, M., Uyeda, S., Foucher, J. P., & Sibuet, J. C. (1989), Heat flow anomaly in the middle Okinawa Trough, *Tectonophysics*, *159*(3-4), 307–318. https://doi.org/10.1016/0040-1951(89)90136-4

841 Zhang, L., Luan, X., Zeng, Z., & Liu, H. (2019), Key parameters of the structure and evolution
842 of the Okinawa Trough: Modelling results constrained by heat flow observations, *Geol. J*,
843 *54*(6), 3542–3555. https://doi.org/10.1002/gj.3356
844